

NUMERICAL STUDY OF TURBULENT CHANNEL FLOWS PERTURBED BY
SPANWISE TOPOGRAPHIC HETEROGENEITY: INNER-OUTER INTERACTIONS
WITHIN LOW- AND HIGH-MOMENTUM PATHWAYS

by

Ankit Awasthi



APPROVED BY SUPERVISORY COMMITTEE:

William Anderson, Chair

Stefano Leonardi

Giacomo Valerio Iungo

Wonjae Choi

Copyright © 2018

Ankit Awasthi

All rights reserved

*This dissertation
is dedicated to my mother.*

NUMERICAL STUDY OF TURBULENT CHANNEL FLOWS PERTURBED BY
SPANWISE TOPOGRAPHIC HETEROGENEITY: INNER-OUTER INTERACTIONS
WITHIN LOW- AND HIGH-MOMENTUM PATHWAYS

by

ANKIT AWASTHI, B.Tech, MS

DISSERTATION

Presented to the Faculty of
The University of Texas at Dallas
in Partial Fulfillment
of the Requirements
for the Degree of

DOCTOR OF PHILOSOPHY IN
MECHANICAL ENGINEERING

THE UNIVERSITY OF TEXAS AT DALLAS

May 2018

ACKNOWLEDGMENTS

Firstly, I would would like to express my sincere gratitude to my supervisor, Dr. William Anderson, for his guidance and support and having the belief in me to complete the project. I also wanted to specially thank Dr. Stefano Leonardi for being such a wonderful teacher. I have really learned a lot from your classes, you have really been an inspiration to me. I am also particularly thankful to Dr. G. Valerio Iungo, who inspired me towards experimental fluid mechanics. In addition, I would also like to thank my committee members for providing comprehensive, insightful comments that led to a much-improved manuscript. Lastly I would like to thank the Air Force Office of Scientific Research (Program Manager: Dr. D. Smith) for funding this project under Grant No. FA9550-14-1-0101 and FA9550-14-1-0394. Computational resources 286 were provided by the Texas Advanced Computing Center at The University of Texas at Austin and the Office of Information Technology at The University of Texas at Dallas.

April 2018

NUMERICAL STUDY OF TURBULENT CHANNEL FLOWS PERTURBED BY
SPANWISE TOPOGRAPHIC HETEROGENEITY: INNER-OUTER INTERACTIONS
WITHIN LOW- AND HIGH-MOMENTUM PATHWAYS

Ankit Awasthi, PhD
The University of Texas at Dallas, 2018

Supervising Professor: William Anderson, Chair

This work presents a study on secondary flows, driven and sustained due to topographical variations in the domain. The effects of these secondary flows on inner-outer interactions are then analyzed. This type of interaction between the large-scale structures residing in the logarithmic region and the small-scale structures in the near-wall region have been under extensive study recently. And efforts are being made to develop a predictive model for the dynamics of near-wall structures based on the measurements at a certain distance from the wall. Such a model has immense practical implication for large-eddy simulations. Existing work on amplitude modulation has been focused on smooth-wall flow, however recently roughness-induced changes on amplitude and frequency modulation are being studied which provides a better understanding of the interaction in real conditions. Here a similar study is presented using wavelet analysis to examine how spanwise heterogeneity affects the spectral density and correlation profiles, which provides a basis for the understanding of amplitude and frequency modulation. The topography under consideration are two Gaussian mounds placed $2H$ apart, where H is the flow depth, which induce a domain-scale secondary motion in the flow. The counter-rotating vortices are flanked on either side of the topography such that prominent upwelling and downwelling occurs above the low and high roughness

respectively. Two cases with the maximum height of the topography as $h/H = 0.05$ and 0.1 are considered, and the results are compared with a homogeneous roughness case ($h/H = 0$). A change in the inclination angle of coherent structures is observed within downwelling region of the flow, however, it does not diminish inner-outer interactions. The extent to which secondary flows disrupts the distribution of spectral density across constituent wavelengths throughout the depth of the domain are also quantified. It is observed that the outer peak associated with the large-scale motions is preserved within the upwelling zone, but vanishes in the downwelling zone. Single- and two- point correlation profiles for low-, intermediate- and high-resolution are compared which validates the resolution independence. An important observation indicates that the selection of reference location while computing the two-point correlation profiles is quintessential. It is also revealed that the strength of modulation is not determined by the wavelength at which the spectral energy resides, but by a mere presence of energy above the separation scale.

TABLE OF CONTENTS

ACKNOWLEDGMENTS	v
ABSTRACT	vi
LIST OF FIGURES	x
LIST OF TABLES	xii
CHAPTER 1 INTRODUCTION	1
1.1 Introduction	1
1.2 A note on Townsend’s and Taylor’s hypothesis	2
1.3 A note on Inclination Angle	3
1.4 Energy cascade and Kolmogorov’s hypothesis	4
1.5 Low- and high-momentum pathways	5
1.6 Amplitude and Frequency modulation in wall turbulence: Inner-outer interactions	7
CHAPTER 2 LARGE EDDY SIMULATION AND CASES	10
2.1 LES code	10
2.2 Present Study	11
2.3 Wavelet Analysis	14
CHAPTER 3 RESULTS AND DISCUSSION	19
3.1 Flow Visualization	20
3.2 Flow Statistics	24
3.3 Inclination Angle	28
3.4 Pre-multiplied energy spectra	31
3.5 Correlation profiles	35
CHAPTER 4 DOMAIN LENGTH TEST	42
4.1 Cases	43
4.2 Results	43
4.2.1 Time-averaged profiles and PDFs	44
4.3 Profiles	44
4.3.1 Correlation profiles	46

CHAPTER 5 CONCLUSION	49
5.1 Conclusion	49
REFERENCES	51
BIOGRAPHICAL SKETCH	58
CURRICULUM VITAE	

LIST OF FIGURES

2.1	Illustration of the Topographies for (a) Case 1, (b) Case 2 and (c) Case 3. (d) Profiles of height of the topographies for Case 1,2 and 3 in the spanwise plane . . .	12
3.1	Visualization of streamwise velocity fluctuations \tilde{u}' in $x - z$ plane with $\{\tilde{u}', \tilde{w}'\}$ vectors for (a) Case 1, (b) Case 2 and (c) Case 3 respectively at a location which corresponds to the crest.	21
3.2	Visualization of streamwise velocity fluctuations \tilde{u}' in $x - z$ plane with $\{\tilde{u}', \tilde{w}'\}$ vectors for (a) Case 1, (b) Case 2 and (c) Case 3 respectively at a location which corresponds to the trough.	22
3.3	Visualization of time and x -averaged swirl strength $\lambda_{ci} (\langle \tilde{\omega}_x \rangle_{x,t} / \langle \tilde{\omega} \rangle_{x,t})$ contour in $y - z$ plane with $\{\langle \tilde{v} \rangle_{x,t}, \langle \tilde{w} \rangle_{x,t}\}$ vectors superimposed for Cases 1(a), 2(b), and 3(c)	23
3.4	Reynolds stress profiles for Cases 1, 2 and 3 above the (a) crest and (b) trough, Reynolds stress profiles normalized by the friction velocity u_τ for Cases 1, 2 and 3 above the (c) crest and (d) trough; black: case 1, dark gray: case 2 & light gray: case 3	25
3.5	Time-averaged streamwise (a,b,c,d) and wall-normal (e,f) velocity profiles for case 1 (black), case 2 (dark gray) and case 3 (light gray), above the crest (a,c,e) and above the trough (b,d,f)	26
3.6	Spatial correlation map of fluctuating streamwise velocity, $\rho_{xx}(\delta x, y, z; z_{\text{Ref.}})$, in the streamwise-wall-normal plane (see figure 1(d) for $z_{\text{Ref.}}$) above crest and trough respectively. Panels correspond with Case 1 (a,b), Case 2 (c,d) and Case 3 (e,f). Inclination angle (g) for $z_{\text{Ref.}}$ based on (a,c,e)	30
3.7	Color flood contours of spectrograms of \tilde{u}/u_τ based on Fourier mode. Panels corresponds with Case 1 above (a) crest and (b) trough, Case 2 above (c) crest and (d) trough and Case 1 above (e) crest and (f) trough.	33
3.8	Color flood contours of spectrograms of \tilde{u}/u_τ based on Wavelet mode. Panels corresponds with Case 1 above (a) crest and (b) trough, Case 2 above (c) crest and (d) trough and Case 1 above (e) crest and (f) trough.	34
3.9	Amplitude modulation correlation profiles with $z_{\text{Ref.}}/H = 0.5$. Panel correspond with: (a) Case 1 above the crest, (b) Case 1 above the trough, (c) Case 2 above the crest, (d) Case 2 above the trough, (e) Case 3 above the crest, and (f) Case 3 above the trough; black: Resolution $Nz = 128$, dark gray: Resolution $Nz = 96$ and light gray: Resolution $Nz = 64$; solid line denote single point correlation and dashed line represent two-point correlation	36

3.10	Frequency modulation correlation profiles with $z_{\text{Ref.}}/H = 0.5$. Panel correspond with: (a) Case 1 above the crest, (b) Case 1 above the trough, (c) Case 2 above the crest, (d) Case 2 above the trough, (e) Case 3 above the crest, and (f) Case 3 above the trough; black: Resolution $Nz = 128$, dark gray: Resolution $Nz = 96$ and light gray: Resolution $Nz = 64$; solid line denote single point correlation and dashed line represent two-point correlation	37
3.11	Amplitude modulation correlation profiles with $z_{\text{Ref.}}/H = 0.25$. Panel correspond with: (a) Case 1 above the crest, (b) Case 1 above the trough, (c) Case 2 above the crest, (d) Case 2 above the trough, (e) Case 3 above the crest, and (f) Case 3 above the trough; black: Resolution $Nz = 128$, dark gray: Resolution $Nz = 96$ and light gray: Resolution $Nz = 64$; solid line denote single point correlation and dashed line represent two-point correlation	38
3.12	Frequency modulation correlation profiles with $z_{\text{Ref.}}/H = 0.25$. Panel correspond with: (a) Case 1 above the crest, (b) Case 1 above the trough, (c) Case 2 above the crest, (d) Case 2 above the trough, (e) Case 3 above the crest, and (f) Case 3 above the trough; black: Resolution $Nz = 128$, dark gray: Resolution $Nz = 96$ and light gray: Resolution $Nz = 64$; solid line denote single point correlation and dashed line represent two-point correlation	39
4.1	Time-averaged Reynolds stress profiles for Cases 1, 2, 3 and 4; black: $L_x/H = 2\pi$, red: $L_x/H = 4\pi$, green: $L_x/H = 6\pi$ and blue: $L_x/H = 8\pi$	44
4.2	Probability density functions (a,b) and time-averaged streamwise velocity (c,d) for Cases 1, 2, 3 and 4; black: $L_x/H = 2\pi$, red: $L_x/H = 4\pi$, green: $L_x/H = 6\pi$ and blue: $L_x/H = 8\pi$; dashed black line denotes the log law profile.	46
4.3	Amplitude and Frequency modulation correlation profiles. Panel correspond with: (a,c,e,g) R_a at $z_{\text{Ref.}} = 0.5, 0.25, 0.2, 0.125$, (b,d,f,h) R_f at $z_{\text{Ref.}} = 0.5, 0.25, 0.2, 0.125$; black: $L_x/H = 2\pi$, red: $L_x/H = 4\pi$, green: $L_x/H = 6\pi$ and blue: $L_x/H = 8\pi$; solid and dashed lines denote single- and two-point correlation respectively	48

LIST OF TABLES

2.1	Summary of Large-eddy simulation parameters.	13
4.1	Summary of Large-eddy simulation parameters for domain test cases.	43

CHAPTER 1

INTRODUCTION

1.1 Introduction¹

Near-wall turbulence is an interesting area of study due to its ubiquity in various flow conditions ranging from urban landscapes, to pipe flows, to vegetative canopies. Turbulent structures get smaller as the wall is approached (Townsend, 1976), which makes it difficult to measure flow characteristics as Reynolds number increases. There have been extensive studies on flow over smooth walls, which have revealed the presence of coherent structures of different scales, ranging from those associated with the near-wall cycle (Kline et al., 1967; Rao et al., 1971; Bandyopadhyay and Hussain, 1984) to large-scale motions (LSM) (Meinhart and Adrian, 1995; Hutchins and Marusic, 2007a) associated with hairpin packets (Adrian et al., 2000; Adrian, 2007), that reside in different regions of the domain (Kline et al., 1967; Adrian et al., 2000). Roughness, however, ablates the viscous near-wall region by the formation of roughness-scale eddies (Grass, 1971; Raupach et al., 1991; Mejia-Alvarez and Christensen, 2010), resulting in the roughness sublayer (Jimenez, 2004; Castro, 2007). Outer portions of the flow (Townsend, 1976) only experience a momentum deficit, which is induced by the roughness, known as the roughness function, ΔU^+ . Above the roughness sublayer, in the inertial layer, provided $H/h \gtrsim 30$, where H is the flow depth and h is the average element height, Townsend's hypothesis states that the outer-layer flow exhibits a universality and is independent on roughness geometry (Townsend, 1976). The role of roughness is to set the friction velocity, u_τ , and roughness function, ΔU^+ (Townsend, 1976; Jimenez, 2004). Outer-layer similarity has been confirmed by various experiments (Ganapathisubramani et al.,

¹Portions of this chapter have been reproduced with permission from, Awasthi, A. and Anderson, W., 2018, Numerical study of turbulent channel flow perturbed by spanwise topographic heterogeneity: Amplitude and frequency modulation within low- and high-momentum pathways, *Phys. Rev. Fluids* 3, 044602, Copyright 2018 by The American Physical Society.

2003; Hutchins and Marusic, 2007a; Volino et al., 2007; Wu and Christensen, 2007), however some have reported roughness effects on the streamwise velocity fluctuations in the outer layer (Hong et al., 2012).

The presence of elongated low- and high-momentum regions in the outer-portion of the flow with the length, $l_1/H \approx 3$, and inclination angle, $\theta \approx 17^\circ$ has been well established for both smooth- and rough-wall flows. These coherent structures meander substantially in the spanwise direction and coalesce to form very-large-scale motions (VLSMs) (Hutchins and Marusic, 2007a) with length, $l_2/H \approx 21$, where H is boundary layer depth. The presence of VLSMs has been observed in pipes (Ahn et al., 2015; Hellström et al., 2015), channels (Fang and Porté-Agel, 2015; Jacob and Anderson, 2017), and boundary layers (Wu and Christensen, 2007; Ganapathisubramani et al., 2003; Wu and Christensen, 2010). Visualizations of pre-multiplied energy spectra (Hutchins and Marusic, 2007a; Fang and Porté-Agel, 2015; Jacob and Anderson, 2017) reveals the presence of VLSMs in the logarithmic region as a secondary peak in addition to the inner peak. The near-wall regions exhibits a prominent peak termed as the inner-peak (Hutchins and Marusic, 2007a) which is associated with the near-wall cycles (Jimnez and Pinelli, 1999) for smooth wall or roughness-scale eddies (Grass, 1971; Raupach et al., 1991; Mejia-Alvarez and Christensen, 2010) for rough wall.

1.2 A note on Townsend’s and Taylor’s hypothesis

According to Townsend’s similarity hypothesis at high Reynolds number the turbulent flow outside the near-wall region is independent of the wall roughness. However, recently there have been some studies which show that a rough surface can substantially affect turbulent characteristics well outside the near-wall region (Krogstadt and Antonia, 1999; Antonia and Krogstad, 2001). While some have proved Townsend’s similarity hypothesis to be valid (Schultz and Flack, 2009), others have observed that the roughness height, h/H , must have a role in limiting the validity Townsend’s hypothesis (Castro et al., 2006). They claimed

that for a sufficiently small value of roughness height (h/H) Townsend's hypothesis seem to occur but for cases with very rough surface where the height of the roughness is relatively large the effect of roughness is felt beyond the near-wall region.

Another hypothesis of Townsend's (attached eddy hypothesis) states that the eddies attached to the wall grow in proportion to their distance from the wall in a self-similar manner. The hairpin packet scenario proposed by Adrian et al. (2000) clearly supports Townsend's attached eddy hypothesis. They also explained that these hairpin packets with positive or negative velocity fluctuations are the instantaneous visualization of the so-called coherent structures or eddies that are attached to the wall. Therefore if we consider the validity of Townsend's attached eddy hypothesis in a highly rough-wall channel flow such as the present study we can further claim that these eddies must feel the effect of this highly rough surface which is heterogeneous in the spanwise direction.

Taylor's frozen hypothesis states that advection contributed by turbulent circulations themselves is small and therefore the advection of a field of turbulence past a fixed point can be taken to be entirely due to the mean flow. This hypothesis is valid for smooth walls, however, there have been reports that for a rough-wall flow this seems to hold true for region well above the roughness sublayer, but violates within the roughness sublayer (Raupach et al., 1996; Finnigan, 2000; Brunet et al., 1994). Therefore, even though the eddies are still attached to the wall within the roughness sublayer, the flow is not homogeneous due to presence individual roughness elements. This dictates that a temporal correlation cannot be used to determine the attributes of the structures near the wall and hence a two-point spatial correlation is needed to ensure an accurate estimation.

1.3 A note on Inclination Angle

The presence of coherent structures in the near-wall and log-region for both smooth (Adrian et al., 2000) and rough wall (Jimenez, 2004) has been confirmed by numerous studies over

the past years. These coherent structures/hairpin packets which are attached to the wall are inclined at an angle relative to the wall. The inclination angle of these coherent structures for a smooth-wall has been reported to be in a range $12^\circ - 15^\circ$ (Adrian et al., 2000) which increases as we move away from the wall. Although the canonical value of the inclination angle of these hairpin packets is considered to be relatively consistent for a smooth wall other studies have shown that this value changes drastically depending on the roughness characteristics and topographic variations. Krogstad and Antonia (1994) computed two-point correlation in the same plane for a smooth and rough wall. They reported that the correlation contour were inclined at an average value of 10° for the smooth wall and 38° for a rough wall. Coceal et al. (2007) measured the inclination angle using two point velocity correlations for a flow over regular array of cubical roughness. They reported that the mean inclination angle decreases sharply with height from 21.6° to 14.4° . These studies imply that the inclination angle of coherent structures in a rough-wall flow exhibit a behavior different from those in a smooth-wall. Also, that the inclination angle in the roughness sublayer for a rough-wall flow is highly dependent on the topographical arrangement and surface complexity but is nonetheless always greater than canonical smooth-wall flows.

1.4 Energy cascade and Kolmogorov's hypothesis

According to Kolmogorov's hypothesis there exists a scale below which the only parameters that affect the flow are rate at which small scales receive energy from the larger-scales (T_E) and kinematic viscosity, ν . And since, the dissipation rate, ϵ , is determined by the energy transfer rate, T_E , these two rates are nearly equal, i.e., $\epsilon \approx T_E$. Therefore the structure of any turbulent flow reflects the local balance of production, transport and dissipation of turbulent kinetic energy. The transfer of energy is best explained by the mechanism of energy cascading (Richardson 1922). According to Richardson the kinetic energy enters turbulence (through the production mechanism) at the largest scales of motion. This energy is then

transferred to smaller and smaller scales, until, it is dissipated by viscous actions at the smallest (Kolmogorov) scales.

Guala et al. (2011), visualized the low-pass filtered velocity (which corresponds to VLSM) and local dissipation (ϵ) time series at $z^+ = 288$. A probabilistic analysis revealed that both conditional average of dissipation and distribution of rare strong dissipation events are more probable during large-scale velocity excursions, as compared to negative events. This clearly shows a modulation effect of large-scale structures on the dissipative scale near the wall.

1.5 Low- and high-momentum pathways²

Recent studies have shown that there is a high degree of spanwise heterogeneity in the mean flow when the surface roughness exhibits a prominent spanwise heterogeneity (Mejia-Alvarez and Christensen, 2013; Barros and Christensen, 2014; Anderson et al., 2015). Both experimental and numerical studies have shown that due to spanwise heterogeneity, a mean secondary motion is induced in the flow which enhances the mean streamwise vorticity. The spanwise heterogeneities are in the form of significant mean momentum excesses and deficits, which were named low- and high-momentum pathways, respectively, by Barros and Christensen (2014); Mejia-Alvarez and Christensen (2010); Willingham et al. (2013) (HMP, LMP). Counter-rotating vortices flank these HMPs and LMPs (Mejia-Alvarez and Christensen, 2013). However, there have been different findings on the rotational sense of these counter-rotating vortices. Early studies on secondary flows have reported a positive vertical velocity (upwelling) within the LMP, and a negative vertical velocity (downwelling) within the HMP (Mejia-Alvarez and Christensen, 2013; Willingham et al., 2013; Vanderwel and Ganapathisubramani, 2015). However, in a recent study by Yang and Anderson (2017), it

²Portions of this chapter have been reproduced with permission from, Awasthi, A. and Anderson, W., 2018, Numerical study of turbulent channel flow perturbed by spanwise topographic heterogeneity: Amplitude and frequency modulation within low- and high-momentum pathways, *Phys. Rev. Fluids* 3, 044602, Copyright 2018 by The American Physical Society.

was shown that the spanwise spacing, s_y , normalized by the flow depth (here channel half height), is a suitable parameter to determine whether the outer-layer turbulence will be disrupted by HMPs and LMPs. They showed that for a small spanwise spacing, $s_y/H = 0.64$, the flow patterns are similar to the results reported by earlier studies (Vanderwel and Ganapathisubramani, 2015; Mejia-Alvarez and Christensen, 2013; Willingham et al., 2013). However, as the spanwise spacing is increased above a certain value, $s_y/H \gtrsim 1$, there is reversal in the rotational sense of these counter-rotating vortices. They concluded that for small value of spanwise spacing the streamwise roll cells are set by the roughness sublayer and hence large-scale counter-rotating rolls vanish from the inertial layer. Therefore, the roughness sublayer secondary flows exists for all rough-wall flows, whereas, the existence of inertial layer secondary flow greatly depends on spacing, s_y/H (Yang and Anderson, 2017).

There have been sustained efforts to study secondary flows in open channel (Bradshaw, 2003; Nezu and Nakagawa, 1993; Wang and Cheng, 2005; Vermaas et al., 2011). Experimental studies on turbulent duct flows have offered considerable insights on the existence of secondary flows (Brundrett and Baines, 1964; H.C., 1953; Nikuradse, 1933; Hinze, 1967). With these studies, it was concluded that when the production of turbulent kinetic energy is much greater than the viscous dissipation in a localized region, an advection of turbulent kinetic energy (Hinze, 1967) drives a secondary motion in the flow. The increased production of turbulent kinetic energy is higher near the duct corners, which redistributes the terms responsible for enhancing the mean streamwise vorticity.

Anderson et al. (2015) pointed out the resemblance between ducts flow and rough-wall turbulent boundary layer flows. They suggested, that in the roughness sublayer and logarithmic region of a slowly developing rough-wall turbulent boundary layer (Jimenez, 2004) any advection must occur due to a secondary flow. In their study, they used the transport equations for Reynolds-averaged turbulent-kinetic energy and mean streamwise vorticity to determine that the secondary flows are a product of spatial heterogeneity of Reynolds stress tensor components in the spanwise-wall-normal plane. This led to the conclusion that the turbulent

secondary flows were Prandtl's secondary flow of the second kind (Bradshaw, 2003; H.C., 1953; Brundrett and Baines, 1964; Perkins, 1970; Gessner, 1973).

Jelly et al. (2014); Ahn et al. (2015) performed DNS of turbulent channel flow with super-hydrophobic surface. The surface was modeled as spanwise-alternating regions of no-slip and free-slip boundary conditions. They observed a significant reduction in the turbulence production and Reynolds shear-stress components, which decreased the overall skin-friction coefficient. This decrease in turbulence production was due to the secondary flows induced at the edge of an alternatively varying surface texture.

1.6 Amplitude and Frequency modulation in wall turbulence: Inner-outer interactions³

The affect of large-scale structures (LSM, VLSM) on the small-scale near-wall motions has been under extensive study recently. The influence was seen while observing viscous-scaled near-wall peaks in the spectral density of streamwise velocity, which showed a growth in magnitude with increasing Reynolds number (Klewicki and Falco, 1990; De Graff and Eaton, 2000; Metzger et al., 2001; Metzger and Klewicki, 2001; Marusic and Kunkel, 2003; Hoyas and Jimnez, 2006; Hutchins et al., 2009). This was shown to be due to the increased large-scale energy imparted to the near-wall regions as Reynolds number increases. The near-wall fluctuations are therefore the sum of induced fluctuations from the scales above (Hutchins and Marusic, 2007a). Hutchins and Marusic (2007b), while observing the pre-multiplied energy spectra across the full height of the turbulent boundary layer, found two energetic peaks. The inner peak was associated with the viscous-scaled near-wall cycle of elongated high- and low-speed streaks, while the outer-peak found in the logarithmic region corresponded to the

³Portions of this chapter have been reproduced with permission from, Awasthi, A. and Anderson, W., 2018, Numerical study of turbulent channel flow perturbed by spanwise topographic heterogeneity: Amplitude and frequency modulation within low- and high-momentum pathways, *Phys. Rev. Fluids* 3, 044602, Copyright 2018 by The American Physical Society.

superstructure-type events in the log region (Hutchins and Marusic, 2007b).

Mathis et al. (009a) used Hilbert transformations over the low-pass filtered velocity fluctuations to compute the degree of amplitude modulation with single-point correlation of large- and small-scale filtered velocity fluctuations. They concluded that large-scale structures appeared to amplitude modulate the small-scale fluctuations and showed that during an event of large-scale momentum deficit there are reduced small-scale fluctuations in the near-wall regions, while in a large-scale momentum excess event the small-scale fluctuations are enhanced. And this phenomenon is reversed away from the wall because the small-scale fluctuations tend to align themselves with the large-scale momentum deficit region (Mathis et al., 009a).

These studies on inner-outer interactions led to the development of a predictive model for near-wall dynamics (Mathis et al., 2011). In this model, Mathis et al. (2011), used some essential parameters of turbulent structures, which were determined empirically, to predict the statistics of small-scale velocity fluctuations near the wall. The parameters used were: superposition coefficient, α , inclination angle, θ , modulation parameter, β , and a universal signal, $u^*(z, t)$. This modeling approach has promising implications for large-eddy simulations of wall-bounded flow at high Reynolds number.

Studies on amplitude and frequency modulation prove that the interaction between large- and small-scale structures is undeniable. However, most of these studies were based on smooth-wall flow, which gives us an understanding of the flow dynamics in ideal conditions. Rough-wall turbulence is ubiquitous in all engineering and geophysical flows and hence the affect of roughness on these interaction needs attention. Anderson et al. (2015) presented large-eddy simulation results on channel flow over staggered cubes and homogeneous roughness. The results showed correlation profiles of amplitude modulation that were comparable to those reported by Mathis et al. (009a,b). Also for the case of homogeneous roughness, the roughness sublayer correlation is stronger than in the logarithmic region of a smooth-wall

channel flow. The correlation profiles also showed an acute sensitivity to the spatial location, which is due to the roughness sublayer secondary flows associated with individual roughness elements.

In a recent study, Pathikonda and Christensen (2017) performed an experimental study to see the roughness-induced changes on amplitude and frequency modulation. They concluded that even though the correlation profiles show similar trends as smooth walls, amplitude and frequency modulation is more intense in rough-wall flows. This increased correlation was shown to be due to the roughness-induced secondary motion. In the present work, I perform a similar study to see the affects of topographic height on secondary flows, inclination angle of the coherent structures, and amplitude and frequency modulation.

CHAPTER 2

LARGE EDDY SIMULATION AND CASES

2.1 LES code¹

$$\frac{\partial \tilde{\mathbf{u}}}{\partial t} + \frac{1}{2} \nabla (\tilde{\mathbf{u}} \cdot \tilde{\mathbf{u}}) - \tilde{\mathbf{u}} \times \tilde{\boldsymbol{\omega}} = -\frac{1}{\rho} \nabla \tilde{p} - \nabla \cdot \boldsymbol{\tau} + \mathbf{\Pi} + \frac{1}{\rho} \mathbf{f}, \quad (2.1)$$

where $\boldsymbol{\tau} = \widetilde{\mathbf{u} \otimes \mathbf{u}} - \tilde{\mathbf{u}} \otimes \tilde{\mathbf{u}}$ is the subgrid-scale tensor, $\tilde{\boldsymbol{\omega}} = \nabla \times \tilde{\mathbf{u}}$ is the vorticity, \mathbf{f} is a body force term that imposes drag associated with solid obstacles (Anderson and Meneveau, 2010; Anderson, 2012), $\nabla \tilde{p}$ is the pressure correction, and $\mathbf{\Pi} = \{u_\tau^2/H = 1, 0, 0\}$ is an imposed pressure-gradient forcing, where H is the channel half-height. This code has been diversely used in various flow conditions (Albertson and Parlange, 1999; Porte-Agel et al., 2000; Bou-Zeid et al., 2005; Chester et al., 2007; Calaf et al., 2010, 2011; Anderson et al., 2012; Graham and Meneveau, 2012; Anderson and Chamecki, 2014; Stevens et al., 2014; Wilczek et al., 2015). The present LES code is used to model channel flow where roughness Reynolds number indicates "fully rough" conditions (Jimenez, 2004), $Re_\tau = u_\tau H/\nu \sim \mathcal{O}(10^6)$. In order to maintain a solenoidal velocity field, the divergence of Equation 2.1 is computed. The incompressibility condition, $\nabla \cdot \tilde{\mathbf{u}} = 0$, is then applied, and the resultant pressure Poisson equation is solved with Neumann boundary conditions at the top and bottom of the domain, $\partial \tilde{p}/\partial z|_{z/H=1}$ and $\partial \tilde{p}/\partial z|_{z/H=0}$, respectively. Channel centerline conditions are imposed with zero stress, $\partial \tilde{u}/\partial z|_{z/H=1} = \partial \tilde{v}/\partial z|_{z/H=1}$ and zero penetration, $\tilde{w}(x, y, z/H = 1, t) = 0$. Periodic boundary conditions are imposed on the vertical planes of the domain owing to spectral discretization in the horizontal direction. Surface boundary conditions are implemented via the equilibrium logarithmic law and an immersed boundary method (IBM),

¹Portions of this chapter have been reproduced with permission from, Awasthi, A. and Anderson, W., 2018, Numerical study of turbulent channel flow perturbed by spanwise topographic heterogeneity: Amplitude and frequency modulation within low- and high-momentum pathways, *Phys. Rev. Fluids* 3, 044602, Copyright 2018 by The American Physical Society.

depending on the value of $h(x, y)$. For $h(x, y) = 0$, the stress is set as:

$$\tau_{xz}^w(x, y, t) = - \left[\frac{\kappa U(x, y, z, t)}{\log(z/z_o)} \right]^2 \frac{\bar{\bar{u}}(x, y, z, t)}{U(x, y, z, t)}, \quad (2.2)$$

and,

$$\tau_{yz}^w(x, y, t) = - \left[\frac{\kappa U(x, y, z, t)}{\log(z/z_o)} \right]^2 \frac{\bar{\bar{v}}(x, y, z, t)}{U(x, y, z, t)}, \quad (2.3)$$

where, $z_o/H = 10^{-3}$, is a prescribed roughness length, and $\bar{\bar{\cdot}}$ denotes test filtering (Germano, 1992) which is used to suppress numerical contamination due to localized implementation of the equilibrium logarithmic law (Bou-Zeid et al., 2005). For $h(x, y) > 0$, an IBM method (Anderson, 2012) is used to define \mathbf{f} in Equation 2.1, which has been used successfully in similar studies (Anderson, 2016; Anderson et al., 2015). The deviatoric component of $\boldsymbol{\tau}$ is evaluated using the eddy-viscosity modeling approach, $\boldsymbol{\tau} - (1/3)\boldsymbol{\delta}\text{Tr}(\boldsymbol{\tau}) = -2\nu_t\tilde{\boldsymbol{S}}$, where $\nu_t = (C_s\Delta)^2|\tilde{\boldsymbol{S}}|$ is the turbulent viscosity, C_s is the Smagorinsky coefficient (Smagorinsky, 1963), Δ is the filter size, $\tilde{\boldsymbol{S}} = (\nabla\tilde{\mathbf{u}} + \nabla\tilde{\mathbf{u}}^T)/2$ is the resolved strain-rate tensor, and $|\tilde{\boldsymbol{S}}| = (2\tilde{\boldsymbol{S}} : \tilde{\boldsymbol{S}})^{1/2}$ is the magnitude of the resolved strain-rate tensor. C_s is evaluated using the lagrangian-averaged scale-dependent dynamic model of Bou-Zeid et al. (2005). The simulation has been run for a long period of time, $10^3T \leq R_T \leq 10^4T$, where T is one large eddy turnover time and R_T is the total runtime. This is done to ensure that a sufficiently-large number of structures have advected through the domain during the averaging period (Anderson, 2016; Hutchins et al., 2009). Table 2.1 summarizes the averaging time for all the simulations. As one would expect that the averaging time decreases with increasing resolution, which is a natural outcome of difficulties associated with running the simulation at higher resolution.

2.2 Present Study

In this work LES has been used to model turbulent channel flow over different rough-walls. Two cases with varying topographic height are considered, as shown in Figure 2.1(b,c) and

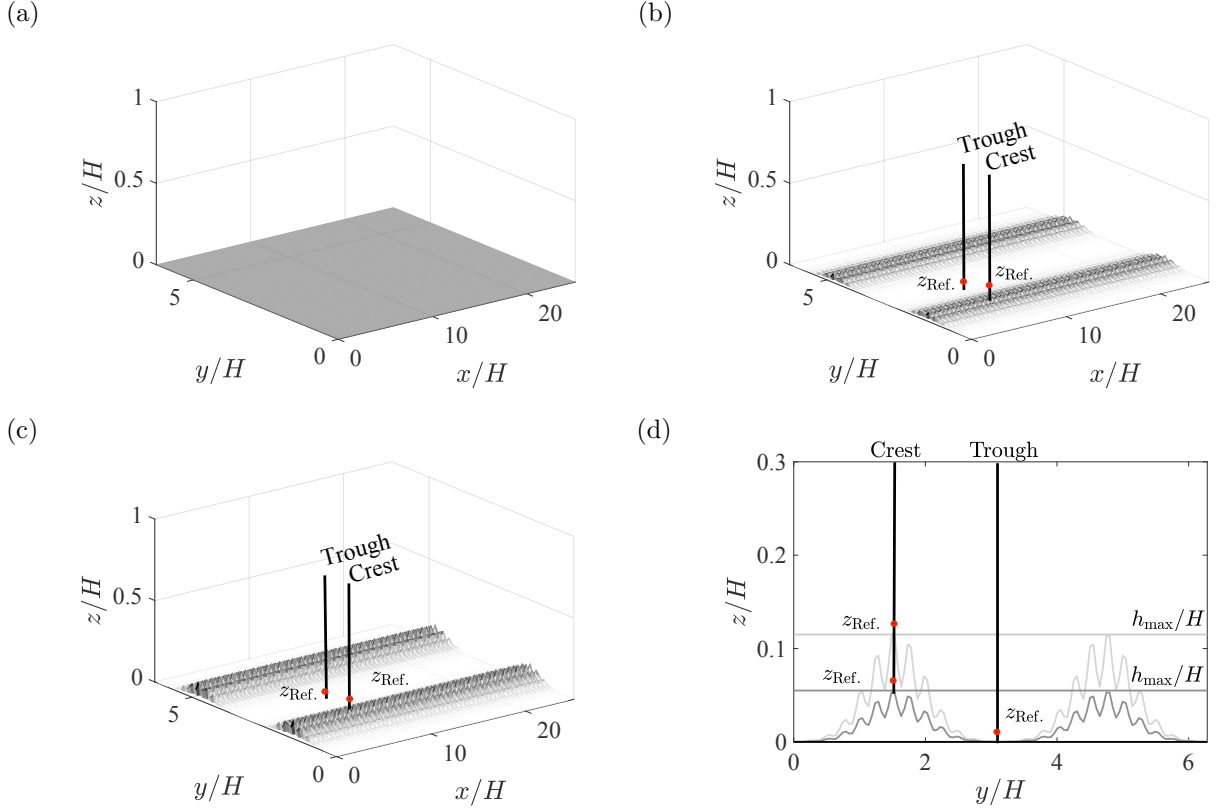


Figure 2.1: Illustration of the Topographies for (a) Case 1, (b) Case 2 and (c) Case 3. (d) Profiles of height of the topographies for Case 1,2 and 3 in the spanwise plane

the results are compared with a turbulent channel flow over homogeneous roughness, which serves as a benchmark for comparison. The drag is modeled via the equilibrium log law through prescription of an aerodynamic roughness length for homogeneous roughness while an Immersed Boundary Method (IBM) (Anderson, 2016) is implemented for cases with varying topographic height. Table 2.1 summarizes the attributes of the surface for different cases. The cases with spanwise heterogeneity were constructed via inner product of two matrices - one with prominent spanwise heterogeneity, the other with streamwise heterogeneity. The height was varied by rescaling the topography such that the maximum height, $h_{\text{max}}/H = 0.05, 0.1$, for Cases 2 and 3 respectively (see Table 2.1). The domain's spatial

Case #	Lx/H	Ly/H	Nx	Ny	Nz	h/H	TU _c /H
Case 1	8 π	2 π	512	128	128	0	2000
Case 2	8 π	2 π	512	128	128	0.05	2000
Case 3	8 π	2 π	512	128	128	0.1	2000
Case 4	8 π	2 π	384	96	96	0	6500
Case 5	8 π	2 π	384	96	96	0.05	6500
Case 6	8 π	2 π	384	96	96	0.1	6500
Case 7	8 π	2 π	256	64	64	0	10000
Case 8	8 π	2 π	256	64	64	0.05	10000
Case 9	8 π	2 π	256	64	64	0.1	10000

Table 2.1: Summary of Large-eddy simulation parameters.

extent, $x, y, z : 0 \leq x/H \leq 8\pi, 0 \leq y/H \leq 2\pi, 0 \leq z/H \leq 1$, where H is the channel half height. The domain is intentionally made longer in the streamwise direction to ensure that the VLSMs, seen as an outer peak (Fang and Porté-Agel, 2015; Mathis et al., 2011; Anderson, 2016) in the pre-multiplied energy spectra, are captured ($8\pi \approx 24$). The friction Reynolds number, $Re_\tau = u_\tau H/\nu \sim \mathcal{O}(10^6)$, indicating that: (1) the simulation is run under "fully rough conditions" (Jimenez, 2004), which would enable comparison with literature datasets under dynamic similarity; and (2) the inertial conditions satisfied the criteria for the existence of large-scale motions (Hutchins and Marusic, 2007a). To ensure the resolution independence, the simulation is carried out at three different resolution: low, intermediate and high. For the lowest resolution $Nx = 256$, for intermediate $Nx = 384$, and for high $Nx = 512$, Table 2.1 provides the details for all the cases. So, Cases 1, 4 and 7 are homogeneous roughness case (Figure 2.1a), Cases 2, 5 and 8 are spanwise heterogeneous case with $h_{\max} = 0.05$ (Figure 2.1b) and Cases 3, 6 and 9 (Figure 2.1c) are spanwise heterogeneous case with $h_{\max} = 0.1$, for different resolutions. This allowed me to assess how domain discretization affects the resultant turbulent statistics and correlation profiles (Anderson, 2016). The next chapter presents a series of results from instantaneous flow visualization to demonstration of topographically driven secondary flows to the outer flow statistics for different cases, which provide a foundation for understanding the correlation profiles obtained using Equations 2.7

to 2.13. An important observation made in this study is that the choice of reference location, $z_{\text{Ref.}}$, while computing the two-point correlation for amplitude and frequency modulation has a profound impact on the trend on the correlation profiles. I computed two-point correlation with different reference locations and found that when the reference location coincides with region where the outer peak is observed, the single- and two-point correlation are similar for a wide range of vertical extent. This result is essentially important while developing a prediction model for near-wall dynamics in a sense that location for the measurement of large-scale statistics will certainly affect the efficacy of the model.

2.3 Wavelet Analysis²

The main advantage of wavelet transform is that it provides joint time-frequency information on input time series. The time-series of streamwise velocity fluctuations is obtained by subtracting the mean velocity from the instantaneous, $\tilde{u}'(x_l, y_l, z, t) = \tilde{u}(x_l, y_l, z, t) - \langle \tilde{u}(x_l, y_l, z, t) \rangle_T$, where $\langle \cdot \rangle_T$ denotes time-average and $\tilde{\cdot}$ denotes a grid-filtered LES quantity. A comprehensive description of the LES code is provided in the following chapter and the nomenclature used here is to provide consistency. In this study, x , y and z denote the streamwise, spanwise and wall-normal directions: u , v and w represent the corresponding velocity components. $\{x_l, y_l\}$ is a discrete point in the horizontal plane where time-series of instantaneous velocity is recorded across the domain height (virtual tower, Anderson et al. (2015)). Figure 2.1 illustrates the positions where the virtual towers are placed. Two spatial location are chosen for the cases with spanwise heterogeneity which correspond with the crest (HMP) and trough (LMP). Although the homogeneous roughness case does not have a crest or a trough, still the same spatial locations is chosen for the sake of comparison. Details of

²Portions of this chapter have been reproduced with permission from, Awasthi, A. and Anderson, W., 2018, Numerical study of turbulent channel flow perturbed by spanwise topographic heterogeneity: Amplitude and frequency modulation within low- and high-momentum pathways, *Phys. Rev. Fluids* 3, 044602, Copyright 2018 by The American Physical Society.

the cases are summarized in the subsequent section. One can refer to Table 2.1 for reference. The large scale component, $\tilde{u}'_L(x_l, y_l, z, t)$, of the velocity field can be obtained by low-pass filtering the velocity fluctuations, $\tilde{u}'(x_l, y_l, z, t)$. Henceforth, I will use $T = \delta_T U_o H^{-1}$ to denote one eddy turnover, where U_o is an "outer" characteristic velocity, H is the flow depth, and δ_T is the (dimensional) time associated with overturning of one domain-scale eddy. The filtering scale is chosen to be, $L = 2T$, which corresponds with the (non-dimensional) time associated with overturning of two domain-scale eddy. This scale is chosen to ensure that only very long structures are considered as large-scale events, which is reasonable considering the streamwise extent, $L_x \approx 24H$. Previous studies of smooth- and rough-wall flows (Mathis et al., 2011; Anderson, 2016) have used filtering scale to be, $L = 1$. Nonetheless, as these studies suggest, the choice of filtering scale has negligible effect as long as the inner and the outer peak are separated by at least an order of magnitude. Provided $L \approx 1$ the result will exhibit only minor differences. The later part of this section is devoted to the method used to quantify how $\tilde{u}'_L(x_l, y_l, z, t)$ modulates the amplitude and frequency attributes of small scale component, $\tilde{u}'_S(x_l, y_l, z, t) = \tilde{u}'(x_l, y_l, z, t) - \tilde{u}'_L(x_l, y_l, z, t)$.

Here, Morlet wavelet function is used to decompose streamwise velocity fluctuations in time-frequency space, which is given by the following expression:

$$\psi(t/t_s) = e^{i\omega_\psi t/t_s} e^{-|t/t_s|^2/2}, \quad (2.4)$$

where t_s is the wavelet timescale normalized by the eddy-turnover time, (T). Joint time-frequency analysis is accomplished via convolution of \tilde{u}' with a spectrum of wavelet functions:

$$\tilde{u}'_*(x_l, y_l, z; t_s, t) = \int_{-\infty}^{\infty} \tilde{u}'(x_l, y_l, z, \tau) \psi\left(\frac{\tau - t}{t_s}\right) d\tau, \quad (2.5)$$

where $\tilde{u}'_*(x_l, y_l, z; t_s, t)$ is decomposed fluctuating velocity in time-frequency space, and t is the independent translation variable in time. Now, the spectral density is obtained by taking the squared modulus of the coefficient obtained after the convolution:

$$E(x_l, y_l, z; t_s, t) = |\tilde{u}'_*(x_l, y_l, z; t_s, t)|^2, \quad (2.6)$$

where $E(x_l, y_l, z; t_s, t)$ is the premultiplied wavelet power spectrum (WPS) at a given time, t , at a discrete point $\{x_l, y_l, z\}$. The normalized time-scale for the wavelets is transformed to an equivalent normalized frequency, f . To obtain the energy content associated with the small-scale energy of the wavelet power spectrum (WPS), I use Parseval's theorem as shown in the work of J. Baars et al. (2015):

$$\sigma_S(t) = \left[\int_{f_c}^{f_N} E(f, t) df \right]^{1/2}, \quad (2.7)$$

where $\sigma_S(t)$ is the instantaneous standard deviation, f_c corresponds to the separation scale between large- and scale- velocity fluctuations, and f_N corresponds to the Nyquist frequency which is half of the sampling frequency f_S . Herein, I set the cut-off frequency, $f_c = L^{-1} = 0.5T^{-1}$, which is consistent with the previously mentioned separation scale. The sampling frequency is chosen to be, $f_S = 10L^{-1} = 0.05T^{-1}$, to ensure that I have a sufficient range of small-scale events. Here, $E(f, t)$ is still the premultiplied wavelet power spectrum (WPS) obtained in Equation 2.6. The spatial subscripts are removed for brevity and the timescale, t_s , is replaced by the frequency scale, f .

Equation 2.7 gives the instantaneous standard deviation, which can be decomposed into a mean and fluctuating component: $\sigma_S(t_i) = \sqrt{\langle u_S^2 \rangle_T} + \sigma'_S(t)$. The aim of this work is to investigate how large scale (low frequency) velocity fluctuations interact with small scales (high frequency). This approach is best suited for such studies, as it provides the information on time-varying small-scale energy in terms of its instantaneous amplitude and frequency. Therefore, this method provides an accurate estimate of the interaction between large and small scales. Now, in order to obtain the large-scale variation of the small-scale amplitude, I low pass-filter the fluctuating component of standard deviation, $\sigma'_S(t_i)$, to obtain $\sigma'_{SL}(t_i)$. Herein, the same separation scale, $f_c = L^{-1} = 0.5T^{-1}$, is chosen. I construct a time series for instantaneous frequency (Boashash, 1992; Cohen, 1989) by computing the first spectral

moment of the instantaneous WPS:

$$f^*(t_i) = \frac{1}{[\sigma(t_i)]^2} \int_{f_c}^{f_N} E(f, t_i) f \log_{10} f d \log_{10} f, \quad (2.8)$$

where,

$$f_S(t_i) = 10^{f^*(t_i)}. \quad (2.9)$$

I obtain the fluctuating component of the instantaneous frequency by subtracting the mean, $f'_S(t_i) = f_S(t_i) - \langle f_S(t_i) \rangle_T$. The fluctuations are low-pass filtered using the same separation scale to obtain the large-scale variation of the small-scale frequency fluctuations, $f'_{SL}(t_i)$. To obtain the correlation coefficient between small and large scales for amplitude and frequency modulation, I correlate the low-pass filtered fluctuating component of the instantaneous amplitude and frequency with the large-scale velocity fluctuations for full depth of the domain:

$$R_a(z; z) = \frac{\langle \tilde{u}'_L(z, t) \sigma'_{SL}(z, t) \rangle_T}{\sqrt{\langle \tilde{u}'^2_L(z, t) \rangle_T} \sqrt{\langle \sigma'^2_{SL}(z, t) \rangle_T}}, \quad (2.10)$$

and

$$R_f(z; z) = \frac{\langle \tilde{u}'_L(z, t) f'_{SL}(z, t) \rangle}{\sqrt{\langle \tilde{u}'^2_L(z, t) \rangle_T} \sqrt{\langle f'^2_{SL}(z, t) \rangle_T}}. \quad (2.11)$$

The correlations, $R_a(z; z)$ and $R_f(z; z)$, reveal the degree of amplitude and frequency modulation of the small-scale structures due to large-scale motion, respectively. This is, however, a single-point correlation and even though large-scale velocity fluctuations near the wall are merely a superposition of low wave-number flow far away from the wall (Mathis et al., 009a), a two-point correlation where the large scale is fixed at a reference point z_{Ref} would reveal this interaction phenomenon much more accurately. Therefore, two-point correlations are also computed, where the reference height z_{Ref} for the large-scale is fixed:

$$R_a(z; z_{\text{Ref}}) = \frac{\langle \tilde{u}'_L(z_{\text{Ref}}, \tau(z; z_{\text{Ref}})) \sigma'_{SL}(z, t) \rangle_T}{\sqrt{\langle \tilde{u}'^2_L(z_{\text{Ref}}, \tau(z; z_{\text{Ref}})) \rangle_T} \sqrt{\langle \sigma'^2_{SL}(z, t) \rangle_T}}, \quad (2.12)$$

and

$$R_f(z; z_{\text{Ref}}) = \frac{\langle \tilde{u}'_L(z_{\text{Ref}}, \tau(z; z_{\text{Ref}})) f'_{SL}(z, t) \rangle_T}{\sqrt{\langle \tilde{u}'^2_L(z_{\text{Ref}}, \tau(z; z_{\text{Ref}})) \rangle_T} \sqrt{\langle f'^2_{SL}(z, t) \rangle_T}}. \quad (2.13)$$

Since the large-scales are fixed at the reference location, $z_{\text{Ref.}}$, when computing two-point correlation, an advective correction must be incorporated on the large scale. This is done to ensure that the large-scale motions (LSMs) which exhibit a positive streamwise inclination and, thus, negative temporal inclination, are correlated appropriately with the small-scale events at differing height. Therefore, $\tilde{u}'_L(z, t)$, used in Equations 2.10 and 2.11 is replaced by $\tilde{u}'_L(z_{\text{Ref.}}, \tau(z; z_{\text{Ref.}}))$, where, $z_{\text{Ref.}}$, is the reference height, $\tau(z; z_{\text{Ref.}}) = t + \lambda(z; z_{\text{Ref.}})$ is the associated time lag and $\lambda(z; z_{\text{Ref.}})$ is the advective correction. Figure 2.1 provides a visual indication of the reference location, $z_{\text{Ref.}}$ (the annotation is only for discussion, and precise value of the reference location is provided in the later section).

CHAPTER 3

RESULTS AND DISCUSSION

This chapter is composed of five sections which provide the results and analyze and discuss its interpretations. Henceforth, the two regions, Crest and Trough, will correspond with the HMP and LMP in the spanwise heterogeneous case. Also, even though Case 1 does not have a crest or a trough, yet, the same spanwise location is chosen for the virtual tower and plane view (streamwise–wall-normal plane) to provide a appropriate comparison. Therefore, for Case 1, those locations will be referred as Section 1 and 2 for identification. Section 3.1 presents instantaneous and Reynolds-averaged flow visualization, which gives an idea on how the attributes of the structures and the flow changes due a prominent spanwise heterogeneity. The results show a qualitative evidence that the inclination angle of meandering coherent structures visualized in the instantaneous flow are altered above the crest while they remain similar to the homogeneous case above the trough. Section 4.3 provides the vertical profiles of Reynolds-averaged first (mean) and second (stress) order statistics computed with the data obtained from the virtual towers, which further highlight major changes to the flows due to spanwise topographic heterogeneity. A more quantitative analysis of structures is presented in Section 3.3 with the spatial correlations, which confirm that, indeed, the structures undergo steeping above the crest and are essentially similar to homogeneous case above the trough. This would explain why the structures undergo a shift in the peak of spectral density across a range of wavelengths. Section 3.4 provides visualizations of premultiplied energy spectra based on Fourier and Wavelet modes at the crest and the trough for Cases 2 and 3 (spanwise heterogeneity) and Section 1 and 2 for Case 1 (homogeneous roughness). Finally, Section 3.5 shows profiles of single- and two-point correlations for modulation of small scale amplitude and frequency due to large scales. Upon comparing the single- and two-point correlation profiles a unique observation was made. The choice of reference height, $z_{\text{Ref.}}$, seems to be very important while computing the

two-point correlations. Four different reference locations were chosen, $z_{\text{Ref.}}/H = 0.25, 0.5$, which revealed that when the reference height coincides with the location of the outer peak, the single- and two-point correlation profiles overlap to a certain degree.

3.1 Flow Visualization¹

The results presented throughout this article are taken from Awasthi and Anderson (2018). To illustrate the effect of spanwise topographic heterogeneity on the inclination of coherent structures, streamwise velocity fluctuations in the $x - z$ plane are presented. Figures above the Crest/Section 1 and Trough/Section 2 are; Case 1 (Figure 3.1 a, 3.2 a), 2 (Figure 3.1 b, 3.2 b) and 3 (Figure 3.1 c, 3.2 c). A more quantitative study on the inclination angle is presented later. The change in the inclination angle is more prominent near the wall and as we move further away from the wall, these structures appear to approach the standard value of $\theta \approx 16^\circ$ (Wu and Christensen, 2007, 2010). Similar findings have been reported in both numerical and experimental studies (Castro et al., 2006; Coceal et al., 2007). Flow over staggered cube arrangements have been studied experimentally by Castro et al. (2006) in a wind tunnel and numerically by Coceal et al. (2007). Both these studies show that roughness affects the inclination angle of coherent structures. They reported an increased mean inclination angle in the roughness sublayer, which decreases sharply with height. The length scale of these coherent structures is reduced above the crest as they get steeper. (Leonardi et al., 2003) performed DNS study over square bars for different packing density and concluded that the structures appear shorter in the streamwise direction relative to the smooth walls, the spanwise extent of these structures was however, increased. Since crest is a "high roughness" location and thus the HMP is anticipated to be located above

¹Portions of this chapter have been reproduced with permission from, Awasthi, A. and Anderson, W., 2018, Numerical study of turbulent channel flow perturbed by spanwise topographic heterogeneity: Amplitude and frequency modulation within low- and high-momentum pathways, *Phys. Rev. Fluids* 3, 044602, Copyright 2018 by The American Physical Society.

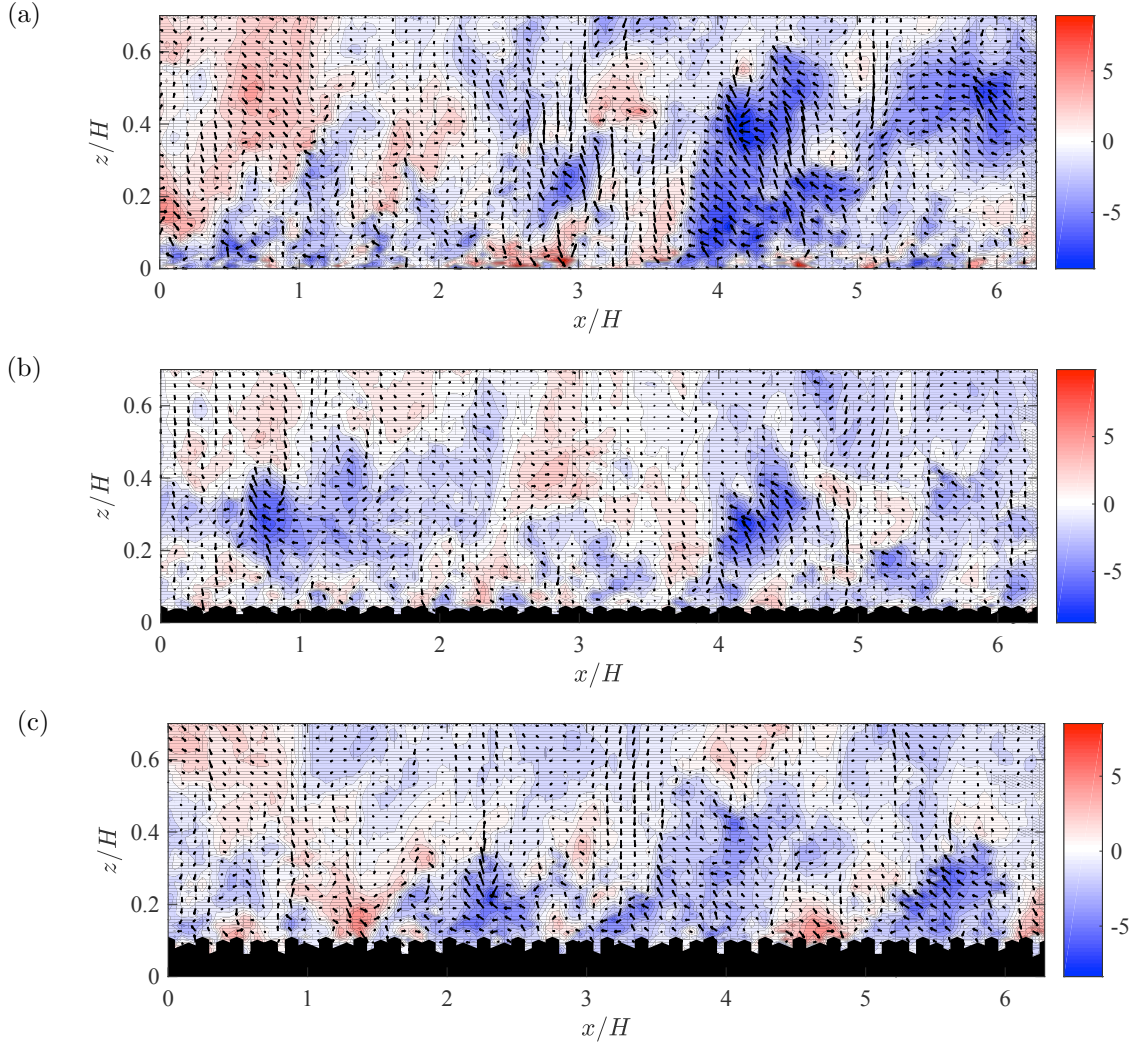


Figure 3.1: Visualization of streamwise velocity fluctuations \tilde{u}' in $x - z$ plane with $\{\tilde{u}', \tilde{w}'\}$ vectors for (a) Case 1, (b) Case 2 and (c) Case 3 respectively at a location which corresponds to the crest.

it (Willingham et al., 2013; Barros and Christensen, 2014; Anderson, 2016). It has also been shown that the secondary flows are the product of a production-dissipation imbalance above the crest, where elevated turbulent kinetic energy (tke) production above the crest necessitates a downwelling of low- tke fluid from the outer region (Hinze, 1967). (Hutchins and Marusic, 2007a).

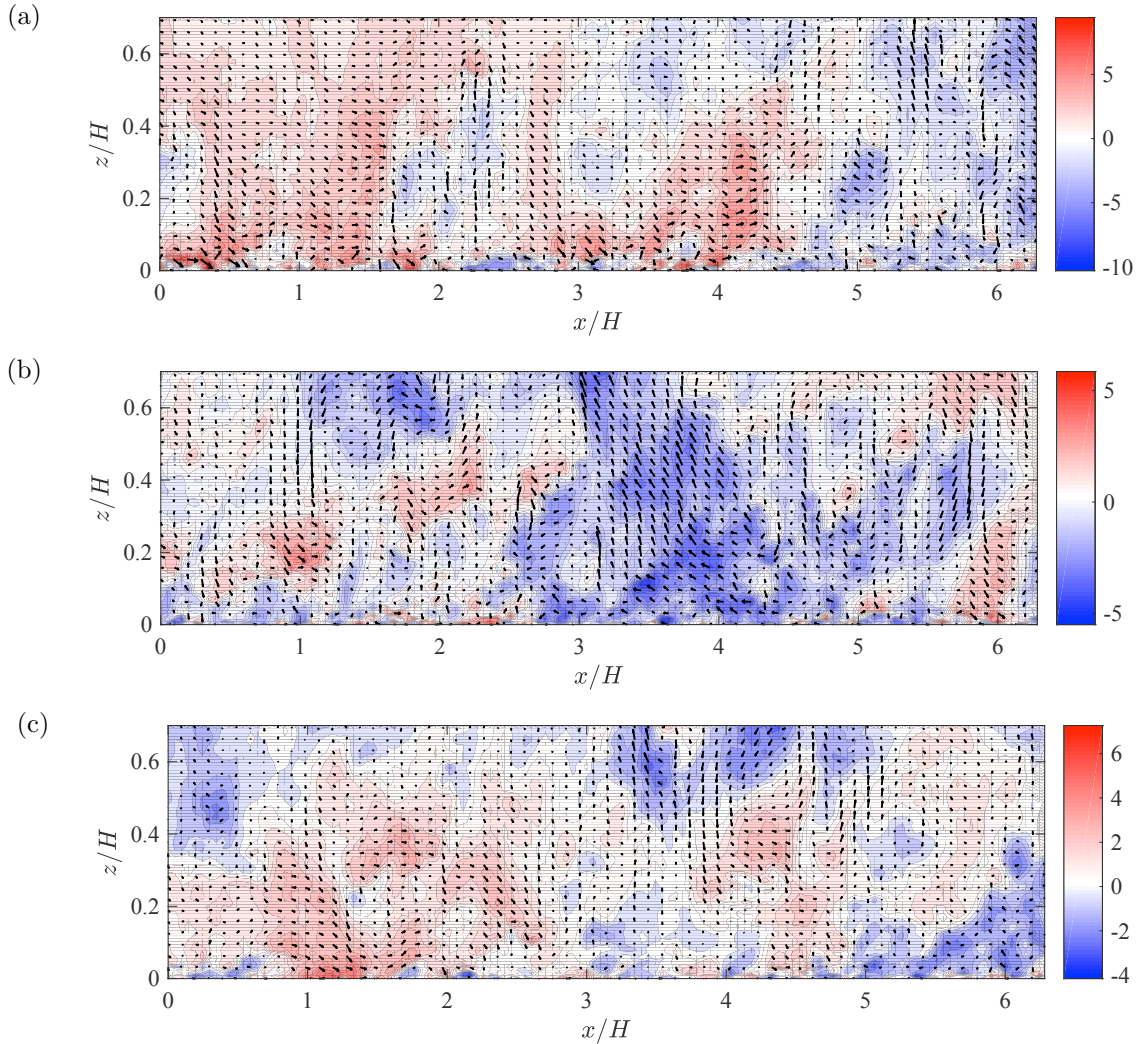


Figure 3.2: Visualization of streamwise velocity fluctuations \tilde{u}' in $x - z$ plane with $\{\tilde{u}', \tilde{w}'\}$ vectors for (a) Case 1, (b) Case 2 and (c) Case 3 respectively at a location which corresponds to the trough.

And, a vigorous mixing of fluid is anticipated above the crest which results in the steepening of structures. Similar quantity is shown in Figure 3.2 (a-c) but at a spanwise location corresponding to the domain trough for Cases 2 and 3 (the homogeneous roughness case does not have a "crest" and "trough" but the same transects are presented to promote consistency with other cases). Above the trough, where the flow exhibits a mild upwelling (Willingham et al., 2013; Barros and Christensen, 2014), coherent structures meander through the domain

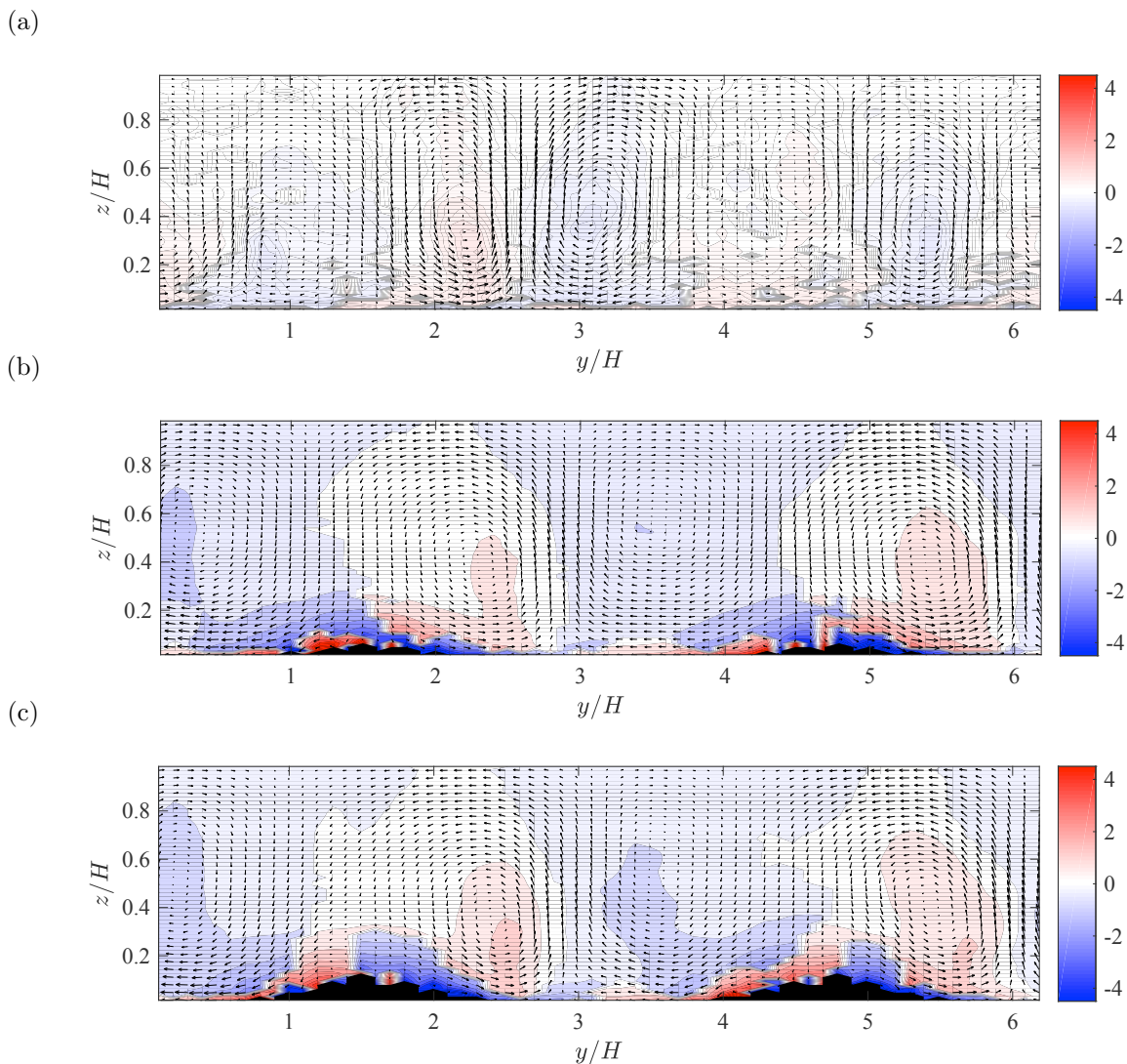


Figure 3.3: Visualization of time and x -averaged swirl strength $\lambda_{ci}(\langle \tilde{\omega}_x \rangle_{x,t} / \langle \tilde{\omega} \rangle_{x,t})$ contour in $y - z$ plane with $\{\langle \tilde{v} \rangle_{x,t}, \langle \tilde{w} \rangle_{x,t}\}$ vectors superimposed for Cases 1(a), 2(b), and 3(c)

and their structural attributes closely resemble those anticipated in canonical shear-driven wall turbulence.

Figure 3.3 shows the time- and streamwise-averaged swirl strength, signed by the mean streamwise vorticity, $\langle \lambda_x \rangle_{x,t}(y, z) \hat{l}_{\tilde{\omega}_x}$ (Wu and Christensen, 2006), where $\hat{l}_{\tilde{\omega}_x} = \langle \tilde{\omega}_{x,t}(y, z) \rangle / \langle \tilde{\omega} \rangle_{x,t}(y, z)$ is the streamwise component of the vorticity unit vector. This figure reveals the existence of alternating low- and high-momentum pathways (Mejia-Alvarez and Christensen, 2010) due

to spanwise topographic heterogeneity. In this study the spanwise spacing, s_y/H , of the Gaussian mounds is set to be greater than 2. Therefore the secondary flows are observed in both roughness sublayer and inertial layer (Yang and Anderson, 2017), this is discussed in detail in Chapter 1 Section 1.5. The upwelling and downwelling motions are present within LMPs and HMPs, respectively, which is consistent with previous finding by Yang and Anderson (2017), although other studies have reported a reversal of flow patterns for smaller spanwise spacing (Vanderwel and Ganapathisubramani, 2015). Another conclusion that can be made from Figure 3.3 is that the strength of secondary flow increases with increasing topographic height which is intuitive since higher topography would result in a more vigorous mixing. Previous studies have revealed that secondary flows have an impact on the dynamics of the mean flow (Willingham et al., 2013; Barros and Christensen, 2014), and in this study it is speculated that these secondary flows also have an impact on the inclination angle of coherent structures.

3.2 Flow Statistics²

Figure 3.4 shows the Reynolds-averaged (total) streamwise-wall-normal momentum flux (Reynolds stress) distribution across the channel height at two location (to show the effect of secondary flow at the crest and trough for Cases 2 and 3). Note that the "total" implies the sum of resolved and subgrid-scale stresses, $\langle \mathbf{u}' \otimes \mathbf{u}' \rangle_T = \langle \tilde{\mathbf{u}}' \otimes \tilde{\mathbf{u}}' \rangle_T + \langle \boldsymbol{\tau} \rangle_T$. For homogeneous roughness case the momentum flux profiles are similar at both locations, which serves as a basis for comparison with cases perturbed by spanwise topographic heterogeneity. For Cases 2 and 3, the Reynolds stress is redistributed due to spanwise heterogeneity, thereby, increasing it above the crest and reducing it above the trough. This imbalance in the

²Portions of this chapter have been reproduced with permission from, Awasthi, A. and Anderson, W., 2018, Numerical study of turbulent channel flow perturbed by spanwise topographic heterogeneity: Amplitude and frequency modulation within low- and high-momentum pathways, *Phys. Rev. Fluids* 3, 044602, Copyright 2018 by The American Physical Society.

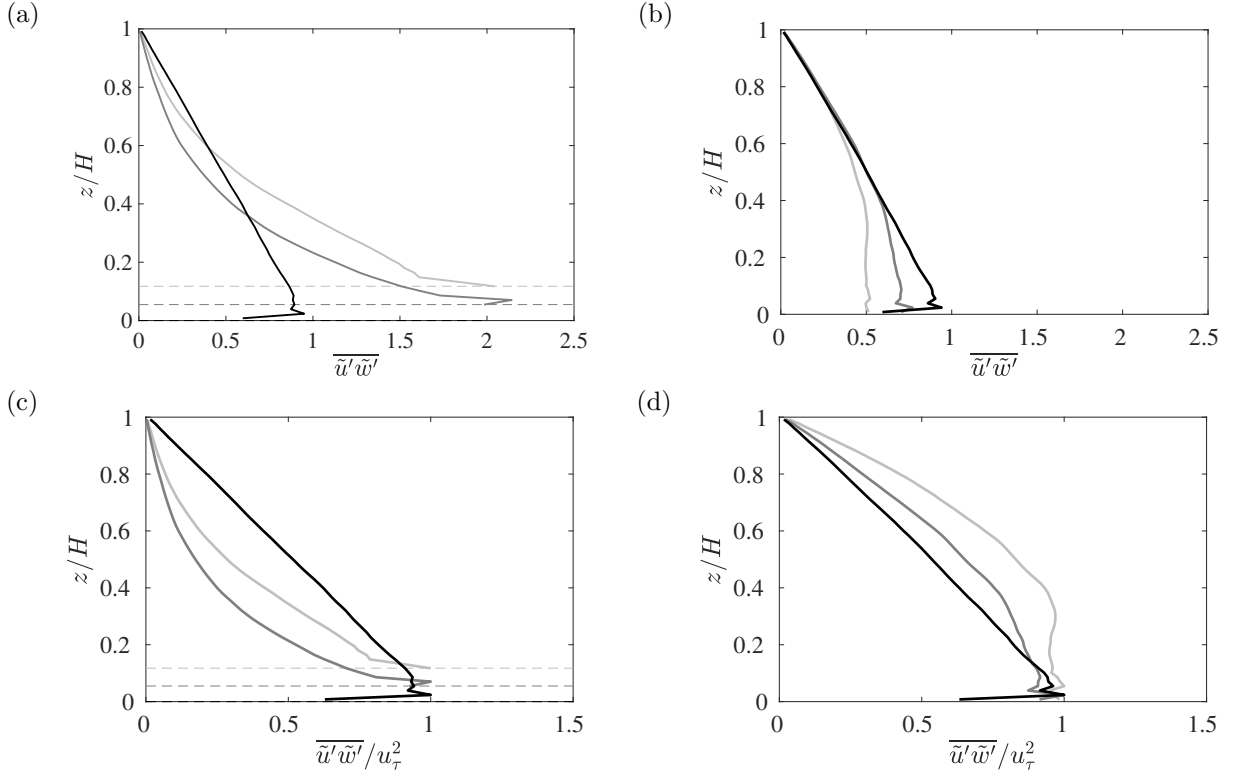


Figure 3.4: Reynolds stress profiles for Cases 1, 2 and 3 above the (a) crest and (b) trough, Reynolds stress profiles normalized by the friction velocity u_τ for Cases 1, 2 and 3 above the (c) crest and (d) trough; black: case 1, dark gray: case 2 & light gray: case 3

Reynolds stress causes the secondary motion in the flow making it Prandtl's secondary flow of the second kind (Anderson et al., 2015). The Reynolds stress profiles shown in Figure 3.4 c and d are normalized by the square of local friction velocity, $u_\tau(y_l)$, which is the maximum value of the square root of total Reynolds stress (resolved $\langle \tilde{u}'\tilde{w}' \rangle_T$ and subgrid $\langle \tau_{xz} \rangle_T$ stresses in the present LES code). Since the Reynolds stress is redistributed in the spanwise direction for Cases 2 and 3, the value of $u_\tau(y_l)$ would be different above the crest and trough, which is unity for homogeneous roughness case. From Figure 3.4 c and d we can conclude that, for Cases 2 and 3 above the crest the larger portion of Reynolds stress is concentrated in the near-wall regions, whereas, above the trough Reynolds stress is dominant further away from the wall.

Figure 3.5 shows time-averaged streamwise and wall-normal velocity components above the

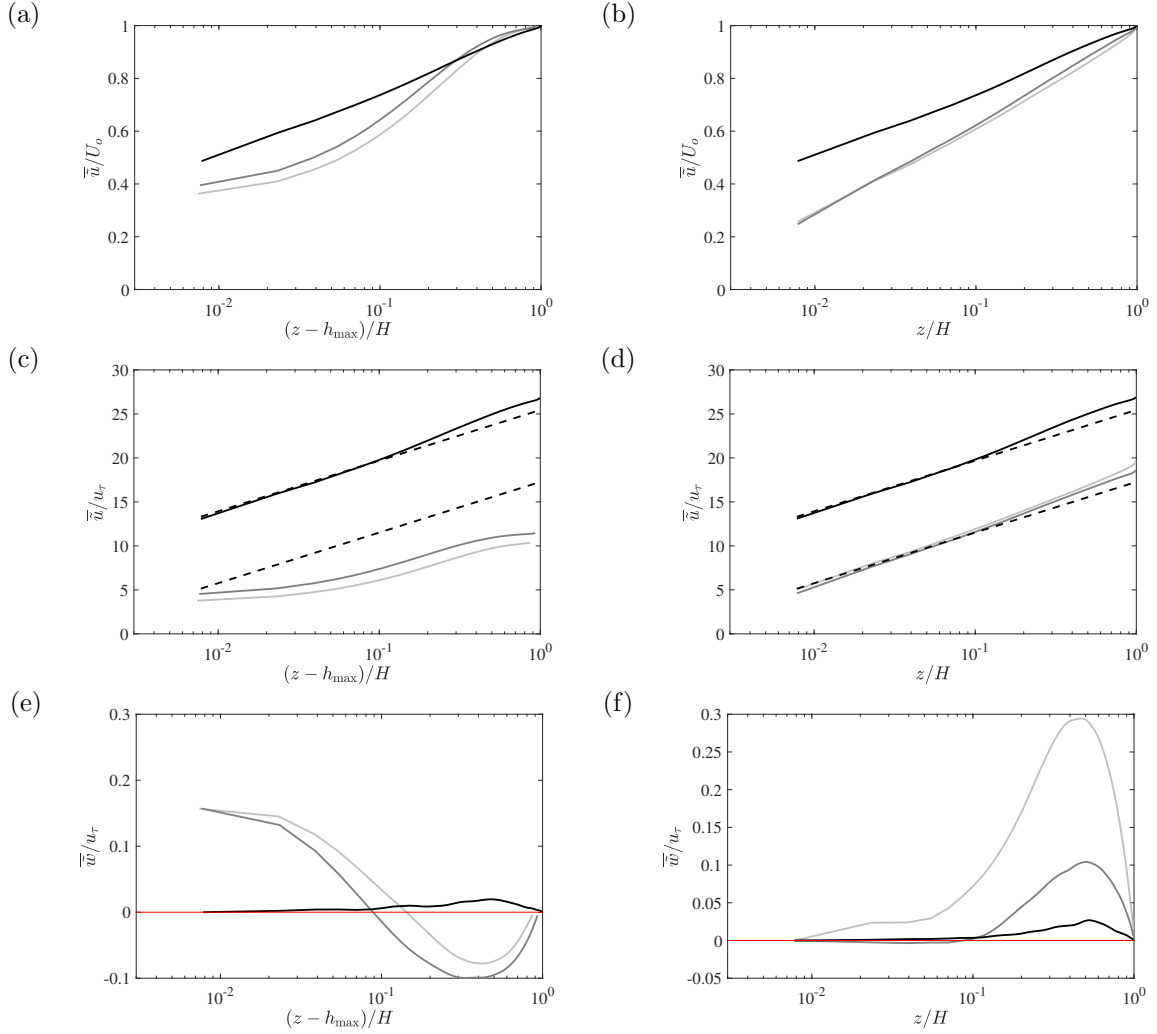


Figure 3.5: Time-averaged streamwise (a,b,c,d) and wall-normal (e,f) velocity profiles for case 1 (black), case 2 (dark gray) and case 3 (light gray), above the crest (a,c,e) and above the trough (b,d,f)

Crest/Section 1 and Trough/Section 2. Figure 3.5 a and b are normalized with outer streamwise velocity, $U_o = \langle \tilde{u} \rangle_T(z/H = 1)$, and Figure 3.5 c, d, e and f are normalized with shear velocity, $u_\tau(y_l)$. From these figures one can observe that the streamwise velocity profile above the crest for Cases 2 and 3 differ significantly from the homogeneous roughness case. Figure 3.5 a reveals that the outer-normalized velocity exhibits a prominent deficit in the lowest 10% of the domain, while, there is a modest (but significant) momentum excess for $z/H \gtrsim 0.2$, relative to the homogeneous roughness case. This is entirely consistent with

the underlying physics responsible for sustenance of the secondary flows, wherein near-wall production of turbulence is strongest and the vertical gradient of $\langle \tilde{u} \rangle(y_l, z)$ is most dramatic. When the vertical profiles of time-averaged streamwise velocity are normalized by the local friction velocity, $u_\tau(y_l)$, the differences become more pronounced. One important thing to note from Figure 3.5 is that the velocity profiles at the two sections for homogeneous roughness case exhibit negligible differences (this result is precisely as expected, and is helpful when drawing comparison to the cases perturbed by spanwise topographic heterogeneity). The dashed black line in Figure 3.5 c and d shows the log-profile using the most widely accepted value of Von Karman constant, 0.41. The streamwise velocity profiles above the crest in Figure 3.5 c, for Cases 2 and 3, also exhibit an absence of the log-region, which in itself is a unique result. Keeping in mind that a key basis for the existence of log-region stems from the idea of existence of a buffer region between the inner viscous-scaled and outer boundary layer-scaled region. The idea here is not to dismiss the already established theories on wall-bounded flows, the evidences for which are pretty compelling, but to question the limits to which they seem valid. Although there have been many studies (Wu and Christensen, 2007; Flack and Schultz, 2010) on rough wall flows which support the outer layer similarity, yet roughness taken into consideration was not as dramatic as the present study. As discussed in the work of Castro et al. (2006) that there must be a critical roughness height beyond which Townsend's hypothesis (which supports the presence of log-region) does not hold true. One point that needs to be stressed here is that even though all these studies were based on the boundary layer flows, and, this study considers a channel flow, yet one can argue that the flow exhibits a similar behavior for the lowest 10% of the flow (George, 2007). Therefore, the absence of log-region above the crest can be considered a genuine outcome of a highly rough wall flow. Another observation that further supports the above statement is that, at the trough, Figure 3.5 d, velocity profile resemble more with the homogeneous roughness case, there is however a vertical shift in the velocity profile which can be associated with overall

drag reduction. Nonetheless, the agreement with the log-profile proves that, in a flow which exhibits a very dramatic variation in roughness (crest and trough in this case), there can be regions associated with "low roughness" where log law holds true, and also regions with "high roughness" where log law does not seem to be valid. Figure 3.3 e and f show the time-averaged vertical velocity, $\langle \tilde{w}' \rangle(y_l, z)/u_\tau$, above the Crest/Section 1 and Trough/Section 2. Firstly, note that for the homogeneous roughness case (Case 1), $\langle \tilde{w}' \rangle(y_l, z)/u_\tau \approx 0$ throughout the depth of the flow, and as the averaging time approaches infinity, the simulations would predict $\langle \tilde{w}' \rangle(y_l, z)/u_\tau \rightarrow 0$. The wall-normal velocity, $\langle \tilde{w}' \rangle(y_l, z)/u_\tau$, which clearly reveal the region of upwelling and downwelling motion in spanwise perturbed case, show, that above the crest $\langle \tilde{w}' \rangle(y_l, z)/u_\tau$ undergoes a change in sign at $z/H \approx 0.1$: for $z/H \lesssim 0.1$, $\langle \tilde{w}' \rangle(y_l, z)/u_\tau > 0$, while for $z/H \gtrsim 0.1$, $\langle \tilde{w}' \rangle(y_l, z)/u_\tau < 0$. The elevation over which, $\langle \tilde{w}' \rangle(y_l, z)/u_\tau < 0$ approximately corresponds with the HMP discussed for Figure 3.5 a, for $z/H \lesssim 0.1$. On the other hand, the zone of downwelling is an outcome of local (roughness sublayer) circulations, which have been well documented in other studies (Goldstein and Tuan, 1998; Yang and Anderson, 2017; Vanderwel and Ganapathisubramani, 2015). Another point to note here is that all the velocity profiles exhibit a monotonic behavior with increasing topographic height, which is a natural outcome of increased topographic effects.

3.3 Inclination Angle³

In the earlier sections it was been highlighted that the topographically driven secondary flows have a dramatic effect on the flow characteristics relative to canonical shear-driven flows. Numerous references were made regarding the steepening of coherent large-scale motions (LSMs) within HMPs (Figure 3.1 and Section 3.1) and its implications on turbulence

³Portions of this chapter have been reproduced with permission from, Awasthi, A. and Anderson, W., 2018, Numerical study of turbulent channel flow perturbed by spanwise topographic heterogeneity: Amplitude and frequency modulation within low- and high-momentum pathways, *Phys. Rev. Fluids* 3, 044602, Copyright 2018 by The American Physical Society.

statistics were discussed. In this section a quantitative analysis on the inclination angle of coherent structures is presented which clarifies many observations made in the previous sections. As mentioned in the Chapter 1, Section 1.2 that the Taylor’s frozen hypothesis is valid for smooth wall, but for rough wall flows it seems to hold true in the outer regions of the flow (Raupach et al., 1996; Finnigan, 2000; Brunet et al., 1994). Therefore, in a highly rough surface such as in this study, where the effect of topography is felt beyond the roughness sublayer, using Taylor’s hypothesis does not seem like a reasonable approach. Therefore, spatial cross correlation of the resolved fluctuating streamwise velocity at spanwise locations corresponding with Crest/Section 1 and Trough/Section 2 are computed:

$$\rho_{xx}(\delta x, y_l, z; z_{\text{Ref.}}) = \frac{\langle \tilde{u}'(x, y_l, z_{\text{Ref.}})u'(x + \delta x, y_l, z) \rangle_{xt}}{\sigma_x(z)^2}, \quad (3.1)$$

where δx is the streamwise separation, $z_{\text{Ref.}}$ is the wall-normal reference elevation, and σ_x is the root-mean-square value of the streamwise velocity fluctuation. The computations of $\rho_{xx}(\delta x, y, z; z_{\text{Ref.}})$ is performed during the simulation and a *posteriori* time averaging is performed, thereby eliminating the need to adopt Taylor’s frozen hypothesis and prescribe an advective velocity. Figures 3.6 a, c and e, and 3.6 b, d and f $\rho_{xx}(\delta x, y_l, z; z_{\text{Ref.}})$ at spanwise locations, y_l , corresponding with the Crest/Section 1 and Trough/Section 2, respectively. Black circles correspond with the maximum correlation,

$$\delta x_m(z; z_{\text{Ref.}}) = \underbrace{\arg \max}_{\delta x} [\rho_{xx}(\delta x, y_l, z; z_{\text{Ref.}})] \quad (3.2)$$

at each wall-normal location (Jacob and Anderson, 2017). The reference location is chosen to be the first grid point above the surface. For Case 1 and the trough for Case 2 and 3 it is at, $z_{\text{Ref.}}/H = 0.01$, while for Case 2 and 3 above the crest it is, $z_{\text{Ref.}}/H = 0.056, 0.12$. The maximum correlation denoted by black circles in the color flood contours are superimposed in Figure 3.6 g and h, corresponding with the Crest/Section 1 and Trough/Section 2 respectively. These figures reveal that as the topographic height is increased, the streamwise

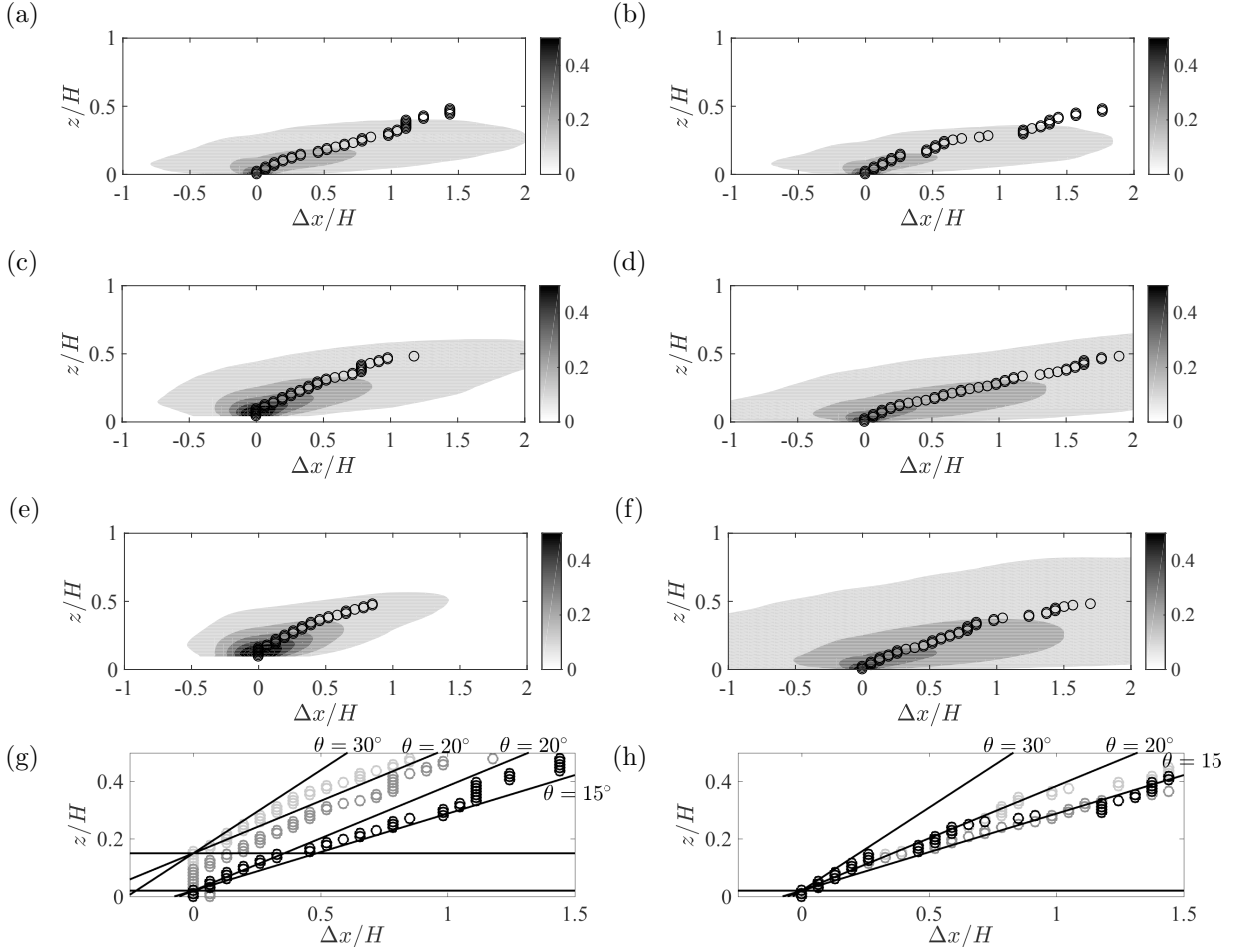


Figure 3.6: Spatial correlation map of fluctuating streamwise velocity, $\rho_{xx}(\delta x, y, z; z_{\text{Ref.}})$, in the streamwise-wall-normal plane (see figure 1(d) for $z_{\text{Ref.}}$) above crest and trough respectively. Panels correspond with Case 1 (a,b), Case 2 (c,d) and Case 3 (e,f). Inclination angle (g) for $z_{\text{Ref.}}$ based on (a,c,e)

correlation above the crest for Case 2 and 3 is diminished, which is also reported by Yang and Anderson (2017). This result is consistent with prior findings on elevated mixing above the high roughness regions, and the corresponding streamwise decorrelation due to vigorous mixing. Above the trough, however, the correlation is similar to the homogeneous roughness case. The streamwise extent of the correlation may not be the most ideal approach to compare the length scale of the structures in this case, since the correlation is performed during simulations and time-averaging window might not have been sufficient. Nonetheless, the

information regarding the inclination angle can be retrieved by the maximum correlation at each elevation. There is an increase in the inclination angle above the crest for Cases 2 and 3, which can be observed in Figure 3.6 g. As the topographic height is increased the inclination angle increases from its canonical range of $15 - 20^\circ$ to nearly 30° near the topography. The inclination angle decreases as we move away from the wall which states that the affect of topohraphy is reduces with the wall-normal elevation. This change in the angle above the crest is due to the induced secondary flow which lifts up these coherent structures. The results for the inclination angle presented above show a similar behavior reported previously (Krogstad and Antonia (1994); Castro (2007); Coceal et al. (2007)), however the magnitude of the angle varies due to the topographical dissimilarities.

3.4 Pre-multiplied energy spectra⁴

Figure 3.7 shows contours of pre-multiplied energy density of resolved (LES) streamwise fluctuating velocity, $k_x E_{\bar{u}'\bar{u}'} / u_\tau^2$, where $k_x = 2\pi/\lambda_x$ is wavenumber and λ_x is wavelength (Hutchins and Marusic, 2007b). These spectrogram are based on projection on Fourier modes, the spectrogram based on wavelets will be presented later in this section. Both spectrogram give the same information however one is represented as a function of wavelength, while the other as a function of frequency, and hence the contours are vertically mirrored version of each other, since $f \propto \lambda^{-1}$. For the homogeneous roughness case (Case 1) we can see a clear separation between the outer- and inner-peak, where the former corresponds to VLSMs while the later corresponds with surface shear layer (Hutchins and Marusic, 2007b). The separation scale of $\lambda_x/H = 2$ is used as a demarcation between the small and large scales. Previous studies have shown that this separation filter has a negligible effect on the

⁴Portions of this chapter have been reproduced with permission from, Awasthi, A. and Anderson, W., 2018, Numerical study of turbulent channel flow perturbed by spanwise topographic heterogeneity: Amplitude and frequency modulation within low- and high-momentum pathways, *Phys. Rev. Fluids* 3, 044602, Copyright 2018 by The American Physical Society.

correlation profiles as long as the outer and inner peak are separated by at least an order of magnitude (Anderson, 2016; Hutchins and Marusic, 2007b). Therefore, any value of separation scale, $\lambda_x/H \approx 1$, would only have very minor variation in the correlation profiles. Two wall-normal locations have been annotated which corresponds with the reference height, $z_{\text{Ref.}}$, chosen while computing the two-point correlation for amplitude and frequency modulation. This helps the reader in understanding the importance of reference location, since one of them strikes precisely at the outer peak, while the other lies beyond the outer peak. This makes it easier while drawing conclusions from the correlation profiles presented in the later sections. Note the spectrogram at two location for homogeneous roughness case (Case 1) in Figure 3.7 are effectively equivalent, and both reveal the presence of spectral plateau over the range, $2 \lesssim \lambda_x/H \lesssim 10^1$. The only reason they are not precisely equivalent, is because they were taken from discrete spanwise locations, and averaging due to spanwise homogeneity was not taken into account (Jacob and Anderson, 2017). Nonetheless, the agreement is quite reasonable as it provides a foundation for assessing the role of topographically-driven secondary flows. Figure 3.7 c, d, and e, f show spectrogram for Case 2 and 3 at spanwise locations corresponding with the crest and trough. Above the crest the distinct outer peak has vanished, and the spectral density has been spread across a range a wavelength without a clear distinction between an outer and inner peak. Although, there is no clear separation between the outer and inner peak, yet there is still some energy residing at wavelengths exceeding the separation scale, $\lambda_x/H = 2$. This observation is important while comparing the correlation profiles in the later section, which demonstrates that a clear outer peak is not the necessary condition to observe the modulation effects, and only the availability of spectral energy beyond the separation scale is sufficient. The observation made earlier regarding the structural similarities between the trough for Case 2 and 3, and the homogeneous roughness case (Case 1) is further validated while observing the spectrograms above the trough, Figure 3.7 d and f. There seems to be no difference between the homogeneous roughness case (Case

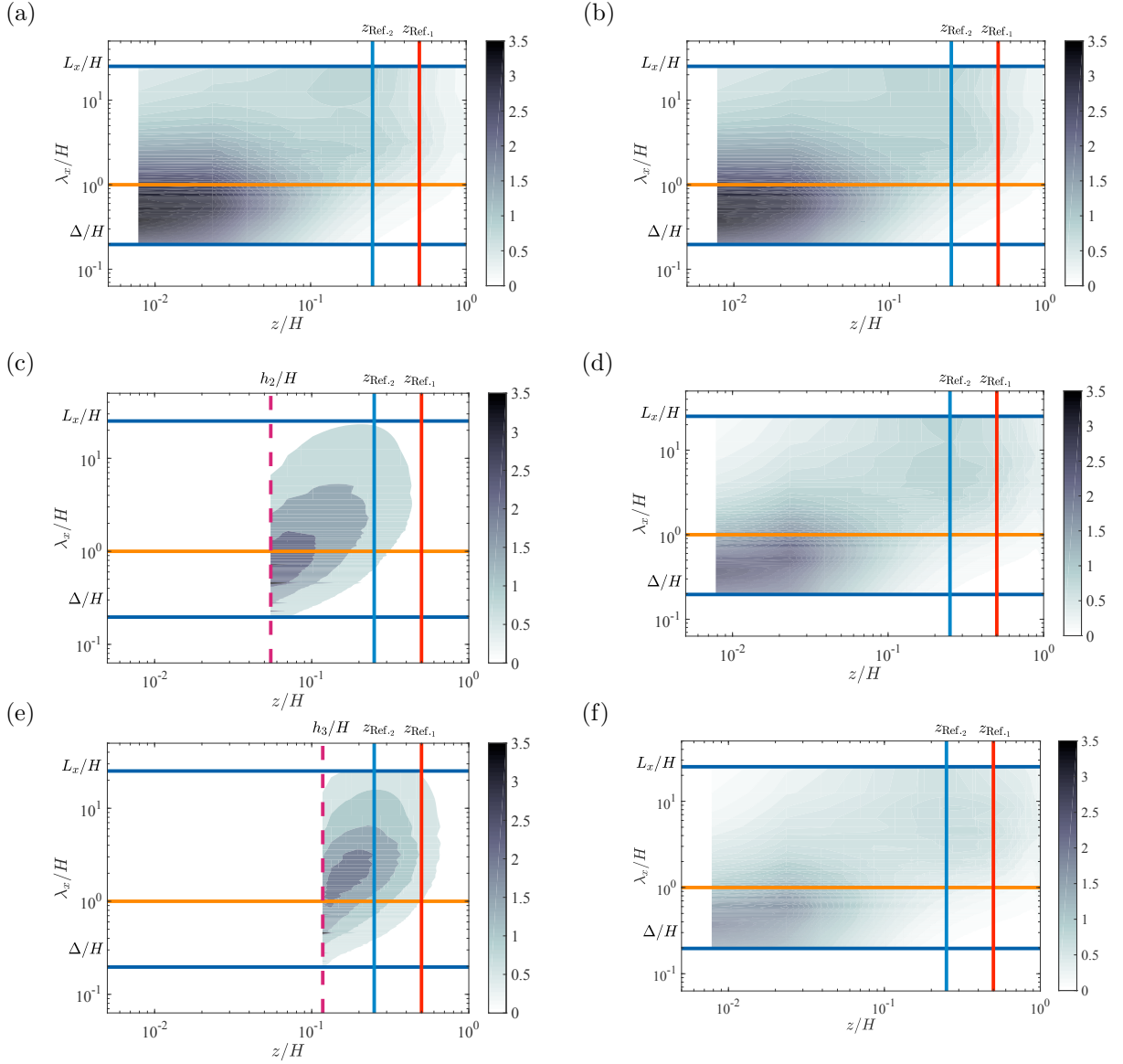


Figure 3.7: Color flood contours of spectrograms of \tilde{u}/u_τ based on Fourier mode. Panels corresponds with Case 1 above (a) crest and (b) trough, Case 2 above (c) crest and (d) trough and Case 1 above (e) crest and (f) trough.

1) and the trough. However, a close observation reveals an important difference: although the spectrograms in Figure 3.7 d and f have a clear outer peak, it has shifted to lower wavelengths ($\lambda_x/H \approx 8$), as opposed to the value, $\lambda_x/H \approx 21$, as seen in the homogeneous roughness case (Case 1).

Although these spectrograms provide all the information required to draw conclusions re-

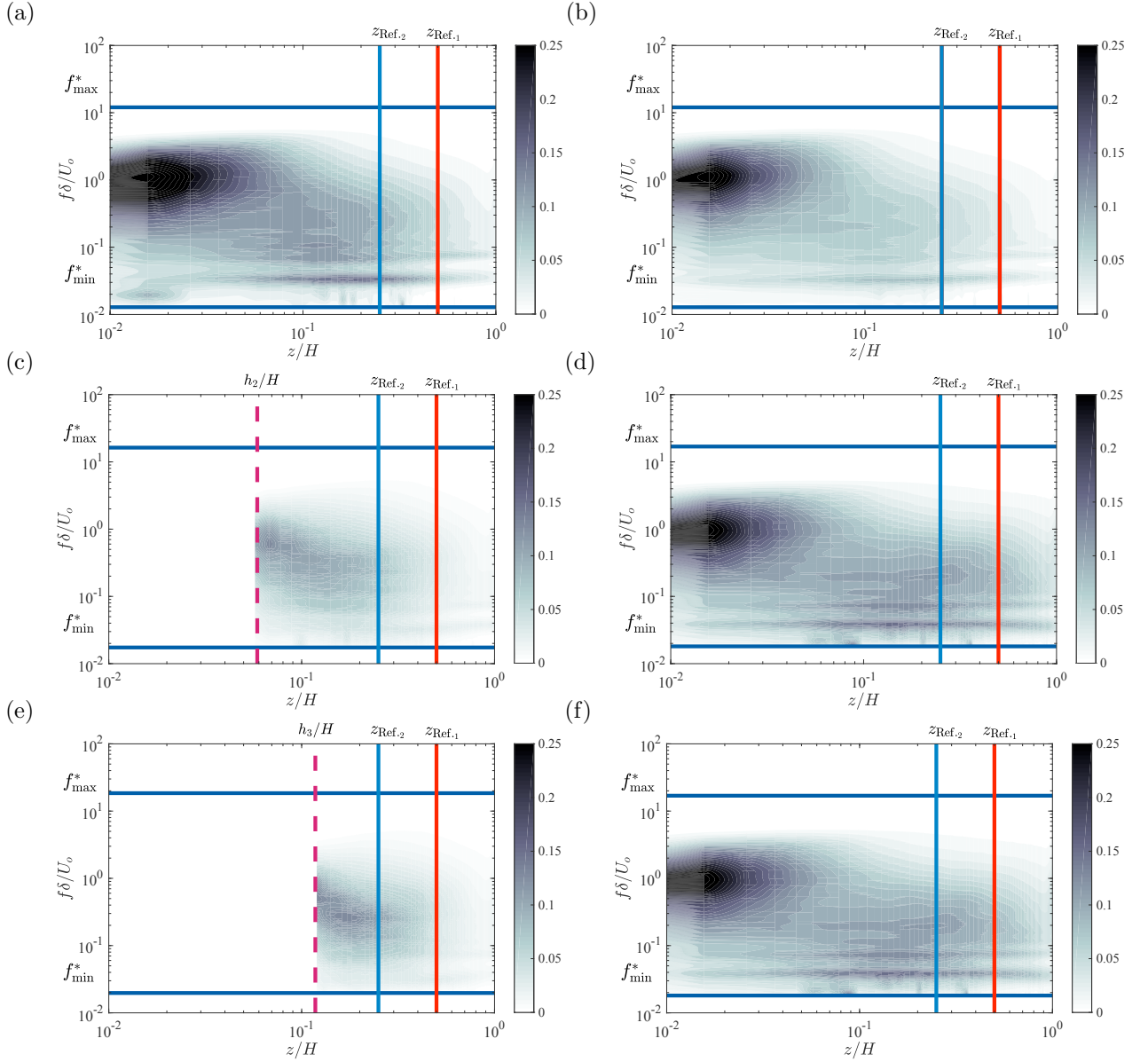


Figure 3.8: Color flood contours of spectrograms of \tilde{u}/u_τ based on Wavelet mode. Panels corresponds with Case 1 above (a) crest and (b) trough, Case 2 above (c) crest and (d) trough and Case 1 above (e) crest and (f) trough.

garding the energy content and the wavelengths at which they reside, but, since the correlation profiles discussed in Chapter 1, Section 2.3 are based on wavelet-based processing of the input time series, the spectrograms of global wavelet power spectrum are also presented. Figure 3.8 shows wavelet-based spectrograms from virtual towers corresponding with

Crest/Section 1 and Trough/Section 2. Wavelet-based spectrograms are generated via processing steps outlined in Chapter 1, Section 2.3, where the wavelet power spectrum, $E(z, f, t)$ is time-averaged, yielding the global wavelet power spectrum, $G(z, f) = \langle E(z, f, t) \rangle_T$. The quantity, $G(z, f)$ is shown in Figure 3.8 above Case 1 (a,b), Case 2 (c,d) and Case 3 (e,f) for two spanwise location. Also, as mentioned earlier, note that the spectrogram obtained via wavelet is just a vertically mirrored version of Fourier-based spectrograms. The wavelet-based spectrograms show slight undulations in the frequency-height space, which is due to insufficiently-long averaging, nonetheless salient features of the flows are captured. A separation scale, $fH/U_o = 1$, based on frequency is also annotated in the figures. The selection of the separation scale for the frequency is based on the relation, $\lambda_x = U_o/f$. One might argue that the use of outer free stream velocity might not be completely justified, however, this is still an open ended question which is not addressed in the present study, and the approach similar to J. Baars et al. (2015) is used.

3.5 Correlation profiles⁵

The solid lines are single-point correlation while the dashed lines correspond with the two-point correlation. Recently Mathis et al. (009a) showed that for a smooth-wall flow the large-scale streamwise velocity fluctuations close to the wall are good substitute for large-scale signature in the log-region. This implies that the large-scale motions away from the wall are merely superimposed upon the wall-parallel smaller-scale close to the wall. One important thing to note here is that the superposition of large-scale on the near-wall region is not instantaneous, i.e., there is a time lag between the occurrence of an event in the log-region and its imprint near the wall. This lag depends on the inclination angle of the large structures

⁵Portions of this chapter have been reproduced with permission from, Awasthi, A. and Anderson, W., 2018, Numerical study of turbulent channel flow perturbed by spanwise topographic heterogeneity: Amplitude and frequency modulation within low- and high-momentum pathways, *Phys. Rev. Fluids* 3, 044602, Copyright 2018 by The American Physical Society.

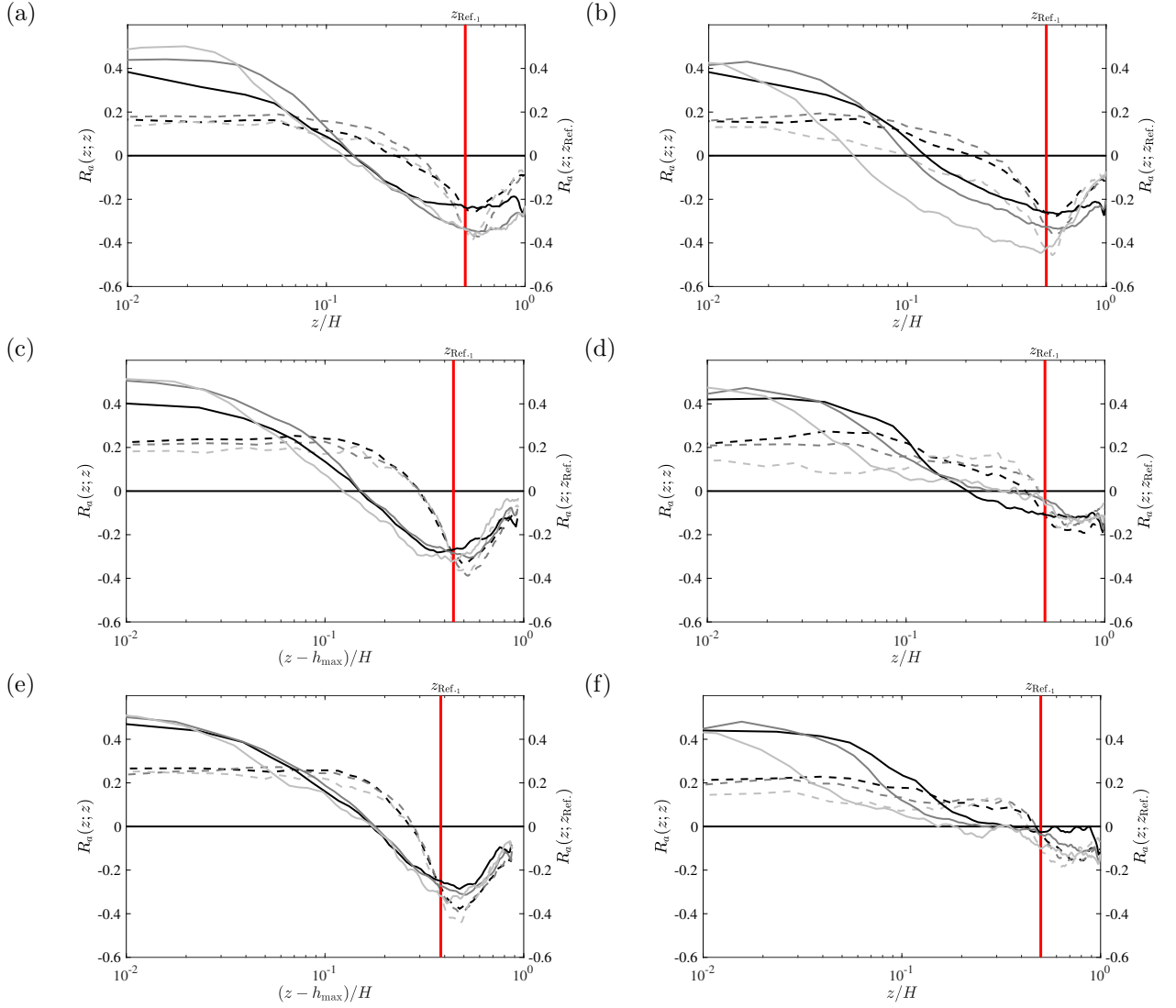


Figure 3.9: Amplitude modulation correlation profiles with $z_{\text{Ref.}}/H = 0.5$. Panel correspond with: (a) Case 1 above the crest, (b) Case 1 above the trough, (c) Case 2 above the crest, (d) Case 2 above the trough, (e) Case 3 above the crest, and (f) Case 3 above the trough; black: Resolution $Nz = 128$, dark gray: Resolution $Nz = 96$ and light gray: Resolution $Nz = 64$; solid line denote single point correlation and dashed line represent two-point correlation

that go well into the log-region but are still attached to the wall. And therefore, a single point correlation would essentially give the same information regarding the modulation effects, yet a two-point correlation, where the reference location, $z_{\text{Ref.}}$, is fixed, would reveal the interaction of large- and small-scale much more accurately. Since establishing resolution

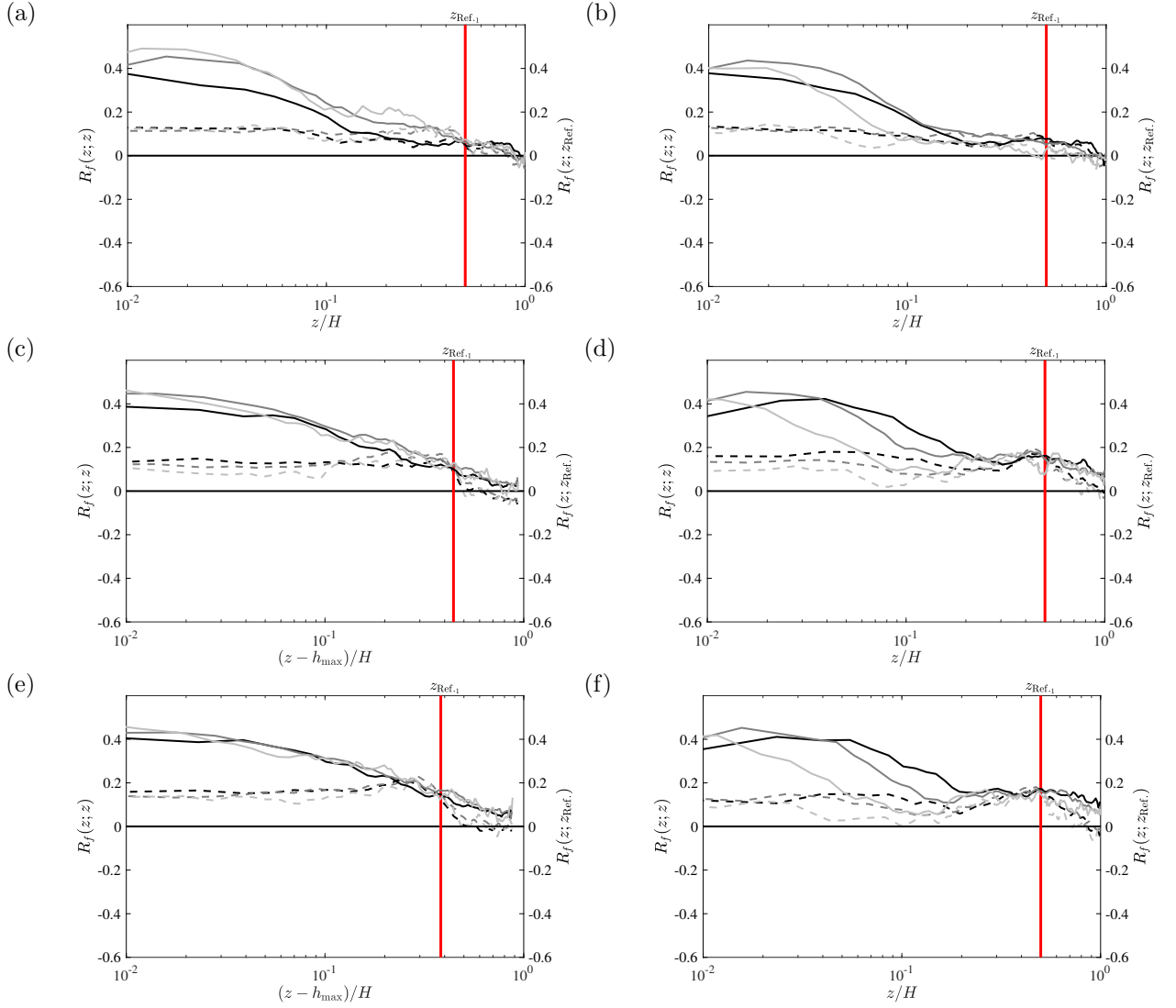


Figure 3.10: Frequency modulation correlation profiles with $z_{\text{Ref.}}/H = 0.5$. Panel correspond with: (a) Case 1 above the crest, (b) Case 1 above the trough, (c) Case 2 above the crest, (d) Case 2 above the trough, (e) Case 3 above the crest, and (f) Case 3 above the trough; black: Resolution $Nz = 128$, dark gray: Resolution $Nz = 96$ and light gray: Resolution $Nz = 64$; solid line denote single point correlation and dashed line represent two-point correlation

independence is of pivotal importance for amplitude and frequency modulation (Anderson, 2016), the profiles across three resolution mentioned in Table 2.1 are also shown (black, dark gray and light gray correspond with low, intermediate and high version of the same flow-topography arrangement). This ensures that the conceptual framework of a predictive model

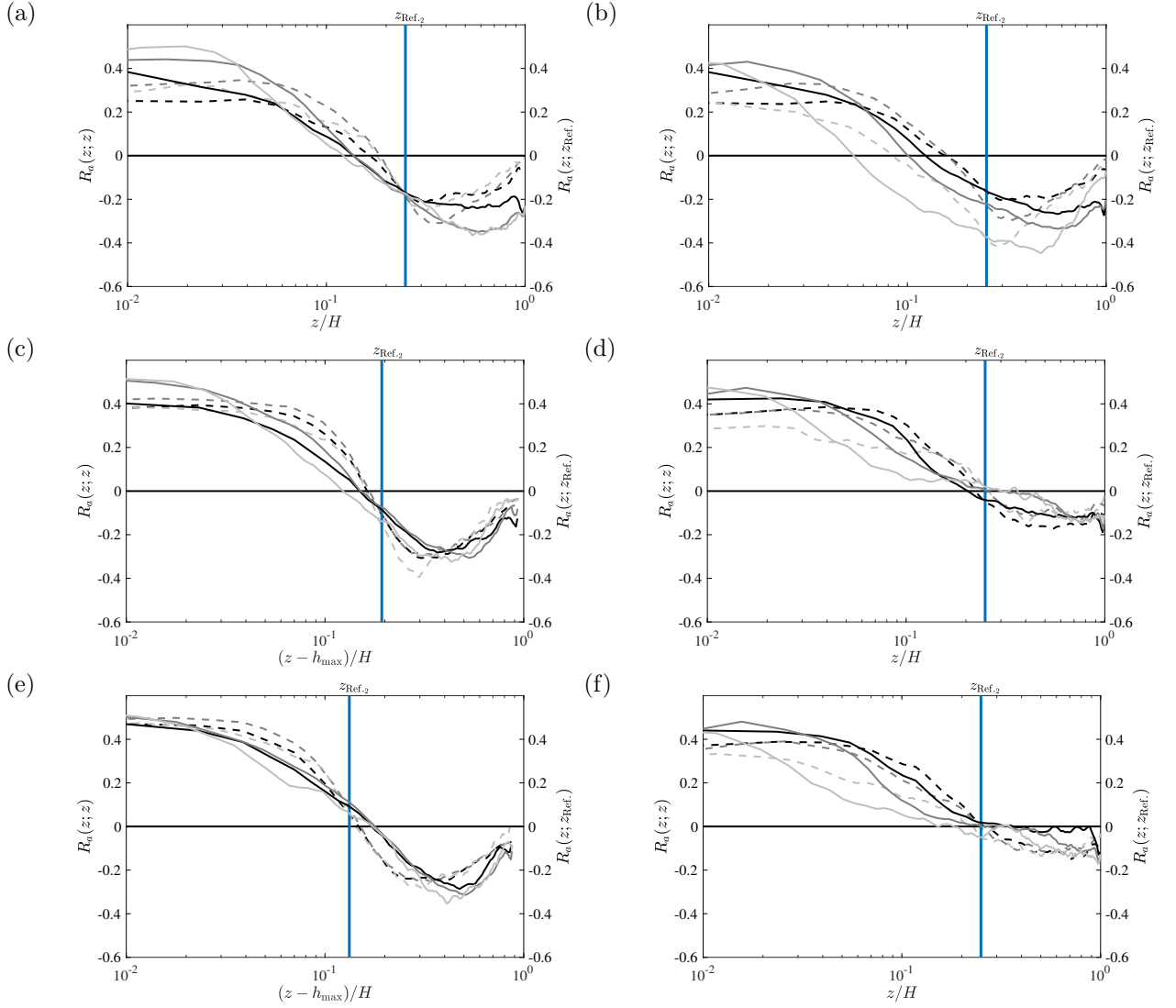


Figure 3.11: Amplitude modulation correlation profiles with $z_{\text{Ref.}}/H = 0.25$. Panel correspond with: (a) Case 1 above the crest, (b) Case 1 above the trough, (c) Case 2 above the crest, (d) Case 2 above the trough, (e) Case 3 above the crest, and (f) Case 3 above the trough; black: Resolution $Nz = 128$, dark gray: Resolution $Nz = 96$ and light gray: Resolution $Nz = 64$; solid line denote single point correlation and dashed line represent two-point correlation

(Mathis et al., 2011) can be utilized in a more general sense. Since the high resolution case requires a very long averaging period, this presents numerical challenges. Nonetheless, the general trend of the profiles is similar to low- and intermediate-resolution cases, also, there is a much clearer agreement between the low- and intermediate resolution cases. This result

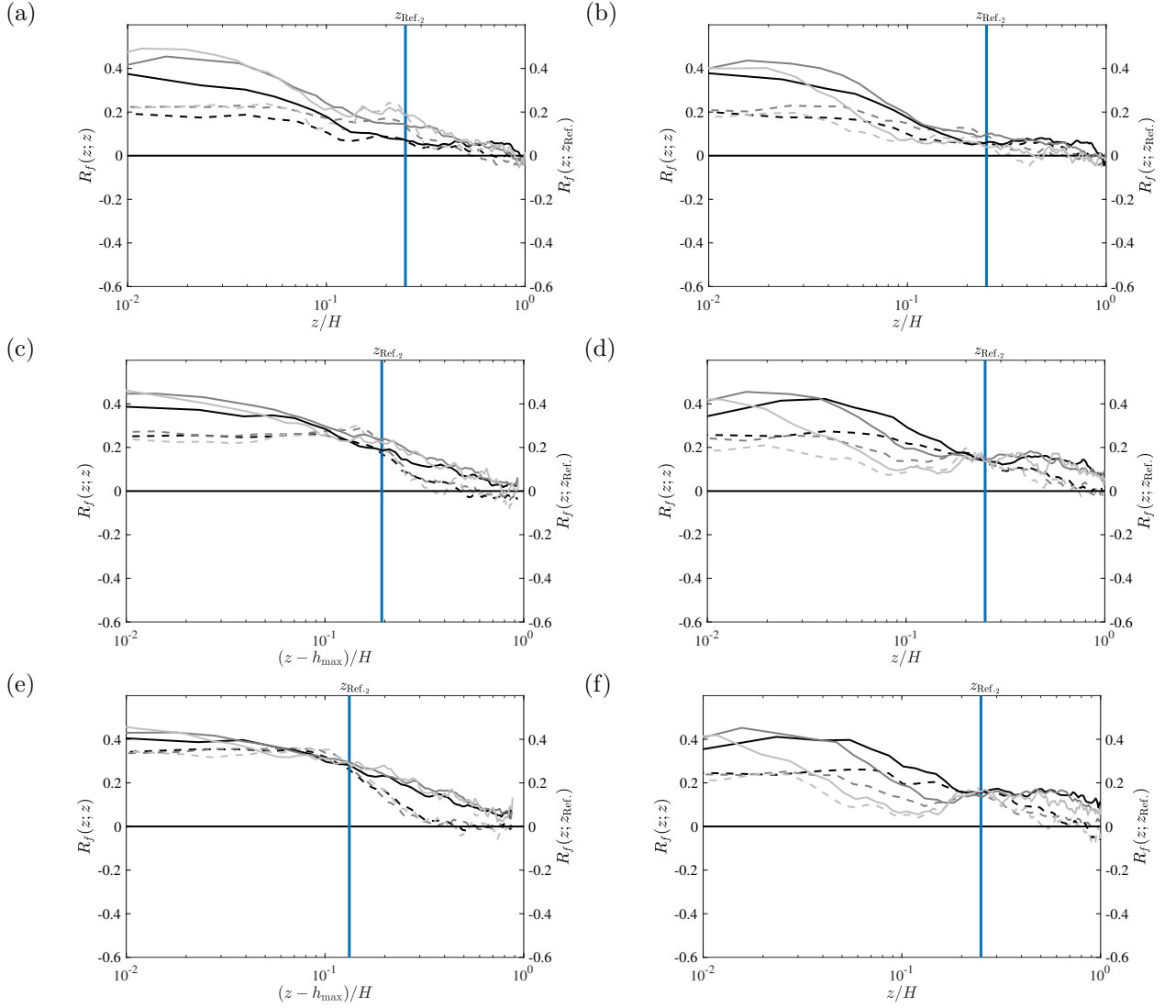


Figure 3.12: Frequency modulation correlation profiles with $z_{\text{Ref.}}/H = 0.25$. Panel correspond with: (a) Case 1 above the crest, (b) Case 1 above the trough, (c) Case 2 above the crest, (d) Case 2 above the trough, (e) Case 3 above the crest, and (f) Case 3 above the trough; black: Resolution $Nz = 128$, dark gray: Resolution $Nz = 96$ and light gray: Resolution $Nz = 64$; solid line denote single point correlation and dashed line represent two-point correlation

is complaint with the conceptual foundations of LES, wherein Reynolds-averaged turbulence quantities should be equivalent even as the subgrid- and resolved-scale contributions vary with varying filter scale. An important thing to observe in all the correlation profiles is that the single- and two-point correlation a equivalent at the reference location, $z_{\text{Ref.}}$. A general

inspection reveals that there is no significant difference in the correlation profiles across the Cases 1, 2 and 3, and all the profile irrespective of its spanwise location appear to be very similar. This is a very surprising result as it was expected that the correlation profiles over "high roughness" should atleast have an observable difference from the those over the "low roughness", considering that the flow statistics are quite different. As shown by Pathikonda and Christensen (2017) the correlation profile over "high roughness" exhibits a higher degree of amplitude modulation than "low roughness" for a small vertical extent. However, there is one point that should be noted: since the abscissa is in log scaling, it is much more reasonable to use $(z - h_{\max})/H$ while showing the correlation profiles, otherwise the comparison between two profiles is not justifiable.

It can be observed from Figure 3.9 that for most part $|R_a(z; z)| \lesssim |R_a(z; z_{\text{Ref.}})|$, which is logical considering that the small scales will be more closely related to the large scale at same elevation. However, there is narrow range, $0.1 \lesssim z/H \lesssim 0.2$, where $|R_a(z; z)| < |R_a(z; z_{\text{Ref.}})|$. Considering the Fourier- and wavelet-based spectrograms (Figure 3.7 and 3.8, respectively), one can observe that, $z_{\text{Ref.1}}/H$, lies above the "outer peak" and the range in which $|R_a(z; z)| < |R_a(z; z_{\text{Ref.}})|$ corresponds with the spectral plateau. Keeping in mind that in the correlations based on the equations mentioned in Chapter 1, Section 2.3 input argument $\sigma'_{SL}(z, t)$ does not change, the difference must be generated by differing large scales at reference location, $u'_L(z_{\text{Ref.}}, \tau(z; z_{\text{Ref.}}))$; the zone of $|R_a(z; z)| < |R_a(z; z_{\text{Ref.}})|$ is thus attributed to the persistent momentum excess above the crest, associated with the HMP. Note, too, that the correlations exhibit a sign reversal at $z/H \approx 0.1$.

Interestingly, for $z_{\text{Ref.1}}/H$, amplitude modulation above the trough (Figure 3.9 b and d) shows much closer agreement between Cases 1, 4 and 7, relative to Cases 3, 6, and 9. It has been argued and demonstrated in all the preceding stages of this work that – atleast for the topographies considered – it is within HMPS (above the crest) that the flow physics are most dramatically perturbed, while LMPs (above the trough) are far less disruptive to the

structural characteristics expected for canonical shear-driven channel flow turbulence.

From Figure 3.7 and 3.8 it is clear that $z_{\text{Ref.1}}/H$ does not intersect the outer peak, and for this reason a second reference location, $z_{\text{Ref.1}}/H$, is considered, which coincides with the outer peak, for homogeneous roughness case and above trough for the spanwise heterogeneous cases. Subsequently, a much closer agreement between single- and two-point correlation is observed as can be seen in Figure 3.11. Despite any distinct outer peak there is still a strong correlation above the crest for Cases 2 and 3. Above the crest, elevated production of turbulence ultimately attenuates large-scale correlation in the flow, and instead spectral density is concentrated in a larger zone. However, the underlying approach to amplitude modulation, which is predicated upon Parseval's theorem, is contingent only upon the variance within the flow, and not the wavelength at which the spectral energy resides.

There is some disagreement between the high-resolution cases, although the overall trends agree. Considering the frequency modulation correlation profiles, Figure 3.10, 3.12, $R_f(z; z) > R_f(z; z_{\text{Ref.}})$, with the exception of $z = z_{\text{Ref.}}$, at which the correlations are by definition equivalent. The single-point correlation continues to rise as the surface is approached, while the two-point correlations remain constant with depth after reaching their upper limit. Moreover, we again see that when the reference location is selected to intersect the outer peak, the single- and two-point correlations agree closely over a large vertical regions, relative to when the reference location does not intersect the outer peak.

CHAPTER 4

DOMAIN LENGTH TEST

The work presented so far discusses the amplitude and frequency modulating effect of VLSMs residing the logarithmic region on the small-scale structures near the wall. As mentioned in Chapter 1, the presence of VLSMs can be observed in the pre-multiplied energy spectra as a secondary peak in the logarithmic region. Moreover, the existence of these VLSMs is predicated upon the two conditions which should be satisfied simultaneously: (1) the streamwise extent of the computational domain must exceed $l_2 \gtrsim 21H$, where H is the flow depth, and (2) the roughness Reynolds number, $Re_\tau \gtrsim 2000$, owing to a fully rough condition. And, although both these conditions were satisfied for cases with spanwise heterogeneity, yet the outer-peak vanishes within the HMP or the "high roughness" region. This was shown in Chapter 3 Section 3.4 via pre-multiplied energy spectra based on both Fourier and Wavelet modes. There was still some spectral density above the separation scale, L or f_c , but there was no discernible difference between the inner and outer peak. This observation prompted, that in a sense the existence of a clear outer peak does not determine the inner-outer interaction. And the absence of a distinct outer peak does not diminish amplitude and frequency modulation. This brings us to the question, is amplitude and frequency modulation a manifestation of the effect of VLSMs on small scale structures or is it more fundamental to turbulent flow, which can explain how the energy is being transferred down the cascade in a systematic manner? The preferential arrangement of small-scales within a momentum excess (HMR) or momentum deficit (LMR) across the domain depth is another important aspect which can be addressed by the generalization of inner-outer interaction. Furthermore, an explanation for the zero crossing of correlation profiles can also be found. But before we can ask such questions, this observation should be validated with more convincing results. This leads to the next section which presents a study of four homogeneous roughness cases with different domain lengths. Of these four cases only one satisfies the condition of sufficiently

Case #	L_x/H	L_y/H	N_x	N_y	N_z	h/H	TU_c/H
Case 1	2π	2π	128	128	128	0	4320
Case 2	4π	2π	256	128	128	0	630
Case 3	6π	2π	384	128	128	0	495
Case 4	8π	2π	512	128	128	0	540

Table 4.1: Summary of Large-eddy simulation parameters for domain test cases.

long streamwise extent required for the existence of VLSMs. The correlation profiles of amplitude and frequency modulation are compared which will give us an idea on how the interaction between large and small scales varies with domain length.

4.1 Cases

Table 4.1 summarizes the LES parameters for the four cases. In order to promote consistency the streamwise discretization is kept constant by increasing the resolution, N_x . The streamwise extent for these cases varies as, $L_x = 2\pi, 4\pi, 6\pi, 8\pi$. One should observe that among the four cases only Case 4, $L_x = 8\pi$, satisfies the condition required for the existence of VLSMs, although, the other condition of, $Re_\tau \gtrsim 2000$ is still satisfied by all the cases. The separation scale, $f_c = 0.5$, is same as used in the preceding chapter and the correlation profiles are computed using the equations mentioned in Chapter 1 Section 2.3.

4.2 Results

A series of results are presented in the next section from probability density to time-streamwise-averaged velocity profiles to pre-multiplied energy spectra based on Wavelet modes to the correlation profiles for amplitude and frequency modulation. All the cases discussed here are turbulent channel flow with homogeneous roughness but with different domain length. As one would expect, the first- and second-order turbulent statistics for all these cases should be essentially the same. The only difference would be that the outer peak

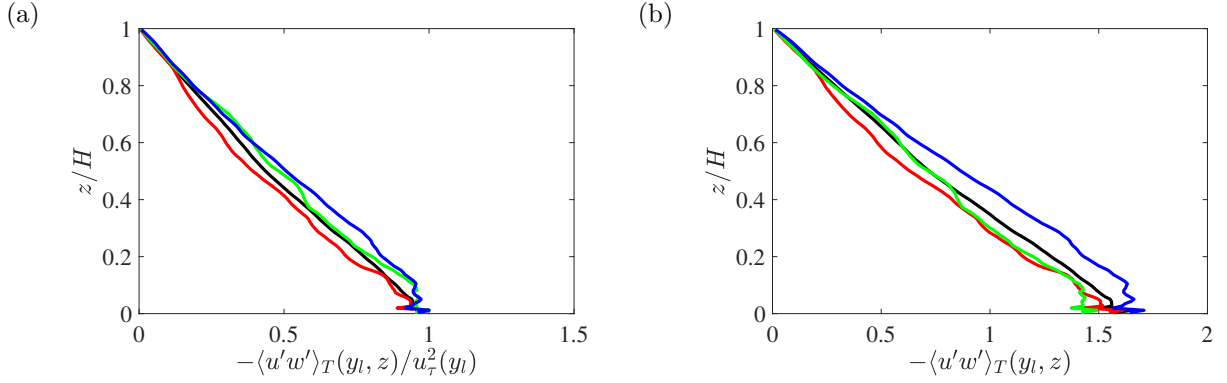


Figure 4.1: Time-averaged Reynolds stress profiles for Cases 1, 2, 3 and 4; black: $L_x/H = 2\pi$, red: $L_x/H = 4\pi$, green: $L_x/H = 6\pi$ and blue: $L_x/H = 8\pi$.

associated with the VLSMs should only be visible for the case with, $L_x/H = 8\pi$. Therefore, the correlation profiles for amplitude and frequency modulation should be most dramatic for the case with maximum domain length, and gets weaker as the domain length decreases. However, as we would see later that this is not true. There is essentially no discernible difference in the correlation profiles among the four cases, which suggests, that even though the conditions for the existence of VLSMs is not met, the interaction between the large- and the small-scales does not get affected. Evidently, this implies that this interaction can be associated with the transfer of energy irrespective of the wavelength/frequency at which it resides. As long as there is presence of some energy above the separation scale there will a correlation between the large- and the small-scales.

4.2.1 Time-averaged profiles and PDFs

4.3 Profiles

Figure 4.1 shows (total) Reynolds stress, the "total" here, with wall-modeled LES, implies the sum of the resolved and subgrid-scale stress, $\langle \mathbf{u}' \otimes \mathbf{u}' \rangle_T = \langle \tilde{\mathbf{u}}' \otimes \tilde{\mathbf{u}}' \rangle_T + \langle \boldsymbol{\tau} \rangle_T$. The different colors denote cases with different domain length: black represents $L_x/H = 2\pi$, red represents $L_x/H = 4\pi$, green represents $L_x/H = 6\pi$ and blue represents $L_x/H = 8\pi$.

Figure 4.1 a and b are normalized by the squared of friction velocity, u_τ , while Figure 4.1 are absolute value of the Reynolds stress. Since the Figure 4.1 a and b are normalized by u_τ , the maximum value of the Reynolds stress reaches one near the wall. The maximum value of the absolute Reynolds stress reaches to 1.5 and hence the friction velocity is approximately unity (which is consistent by definition in the present channel flow). As one would expect these profiles are quite similar, although there are very minor differences, but that is primarily because the simulation has not been run for a very long and the second order statistics needs relatively longer time to converge. One point to stress here is, since these studies are done on a turbulent channel flow and the horizontal boundary conditions are periodic, therefore the domain length should have a negligible impact on the turbulence statistics. However, the aim here is to identify the differences in the correlation profiles of amplitude and frequency modulation. Figure 4.2 a and b shows probability distribution of streamwise and wall-normal velocity fluctuations for different cases. The color for different cases are kept consistent in all the figures, i.e., black: $L_x/H = 2\pi$, red: $L_x/H = 4\pi$, green: $L_x/H = 2\pi$ and blue: $L_x/H = 2\pi$. These distributions are based on the time-series of velocity fluctuations obtained at the second discretized location above the wall. The distributions overlap each other quite precisely which once again confirms that the turbulence statistics are same for flow with different domain lengths. One can observe from Figure 4.2 a that the probability distribution of streamwise velocity fluctuations is positively skewed and the mode is negative. On the other hand the distribution for wall-normal velocity shows zero skewness which makes complete sense considering that the flow is over a channel with homogeneous roughness and hence over a relatively long averaging period the wall-normal velocity would be zero. Figure 4.2 c and d shows time- and streamwise averaged streamwise velocity profiles. Figure 4.2 c is normalized with the outer velocity, U_o and hence the maximum value reaches unity at the top of the domain. Dashed black line in Figure 4.2 denotes the log law profile with $z_o = 10^{-3}$. As expected the streamwise velocity profiles for all the cases overlap each other

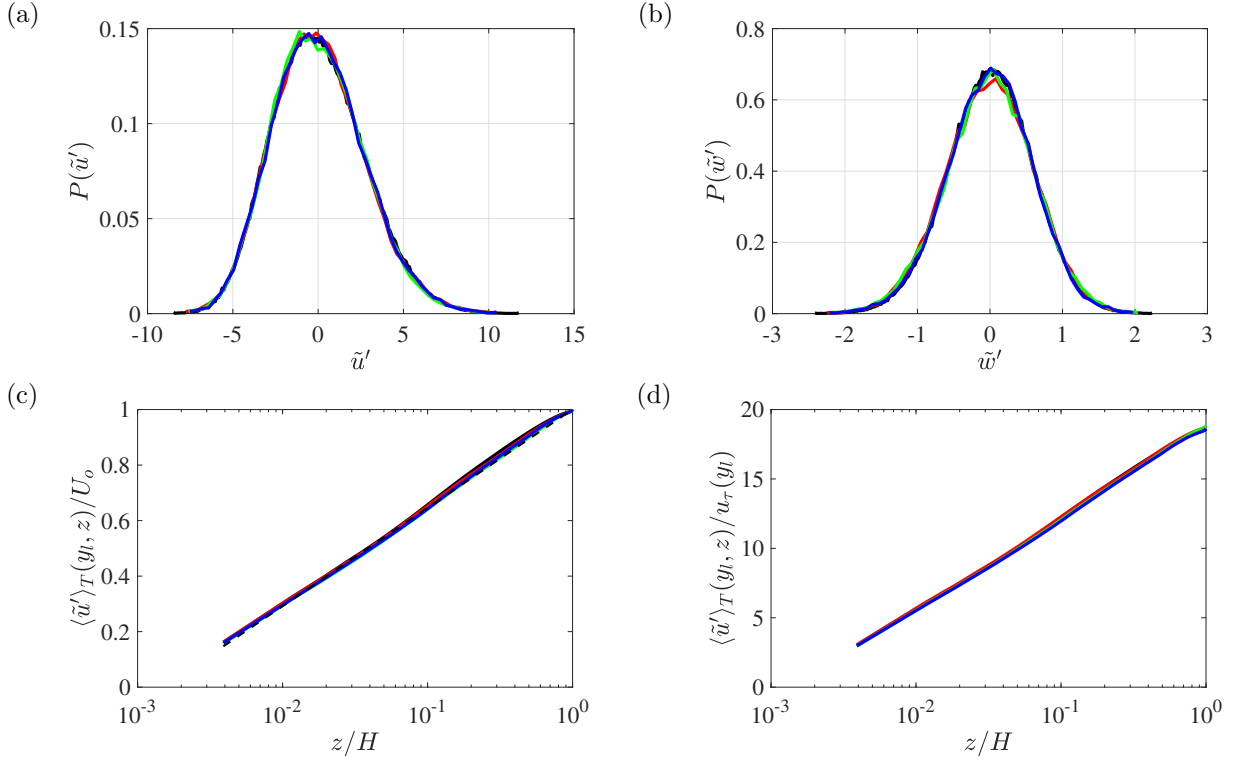


Figure 4.2: Probability density functions (a,b) and time-averaged streamwise velocity (c,d) for Cases 1, 2, 3 and 4; black: $L_x/H = 2\pi$, red: $L_x/H = 4\pi$, green: $L_x/H = 6\pi$ and blue: $L_x/H = 8\pi$; dashed black line denotes the log law profile.

and also with the log law profile. Even when the streamwise velocity is normalized with the friction velocity, u_τ , the profiles are still very similar to each other. The results presented so far in this section provide substantial evidence that the most essential first- and second-order turbulence statistics have negligible impact due to the change in the the domain length. In the next subsection the correlation profiles for amplitude and frequency modulation are presented. Both single- and two-point correlations are computed based on the equations mentioned in Chapter 1 Section 2.3.

4.3.1 Correlation profiles

Figure 4.3 shows the correlation profile for amplitude and frequency modulation based on four different reference locations where the two-point correlations are computed. The ref-

erence location are chosen as, $z_{\text{Ref.}}/H = 0.125, 0.20, 0.25, 0.5$. The purpose of choosing four reference locations is to get an idea on how the two-point correlation varies with reference height and what is the most suitable reference height where the single- and two-point correlation profiles overlap each other. The different colors in the figure denote different cases, which is consistent with the previous figures. One can observe that the correlation profiles for all the cases match quite precisely, which concludes that even if the condition for the existence of VLSMs is not met, there is still an interaction between the large- and the small-scales. Now if one focuses on the two-point correlation profiles it can be observed that as the reference location changes the two-point correlation profile changes. For $z_{\text{Ref.}}/H = 0.5$ the single- and two-point correlation profiles differ significantly, but as the reference location gets closer and closer to the height where an outer peak is supposed to be present, the single- and two-point profiles start to overlap each other. Another important observation that can be made from Figure 4.3 is that reference location where the single- and two-point correlation overlap the most is different for amplitude and frequency modulation. For amplitude modulation the most suitable reference height is $z_{\text{Ref.}}/H = 0.25$, while for frequency modulation the most suitable reference location is $z_{\text{Ref.}}/H = 0.125$.

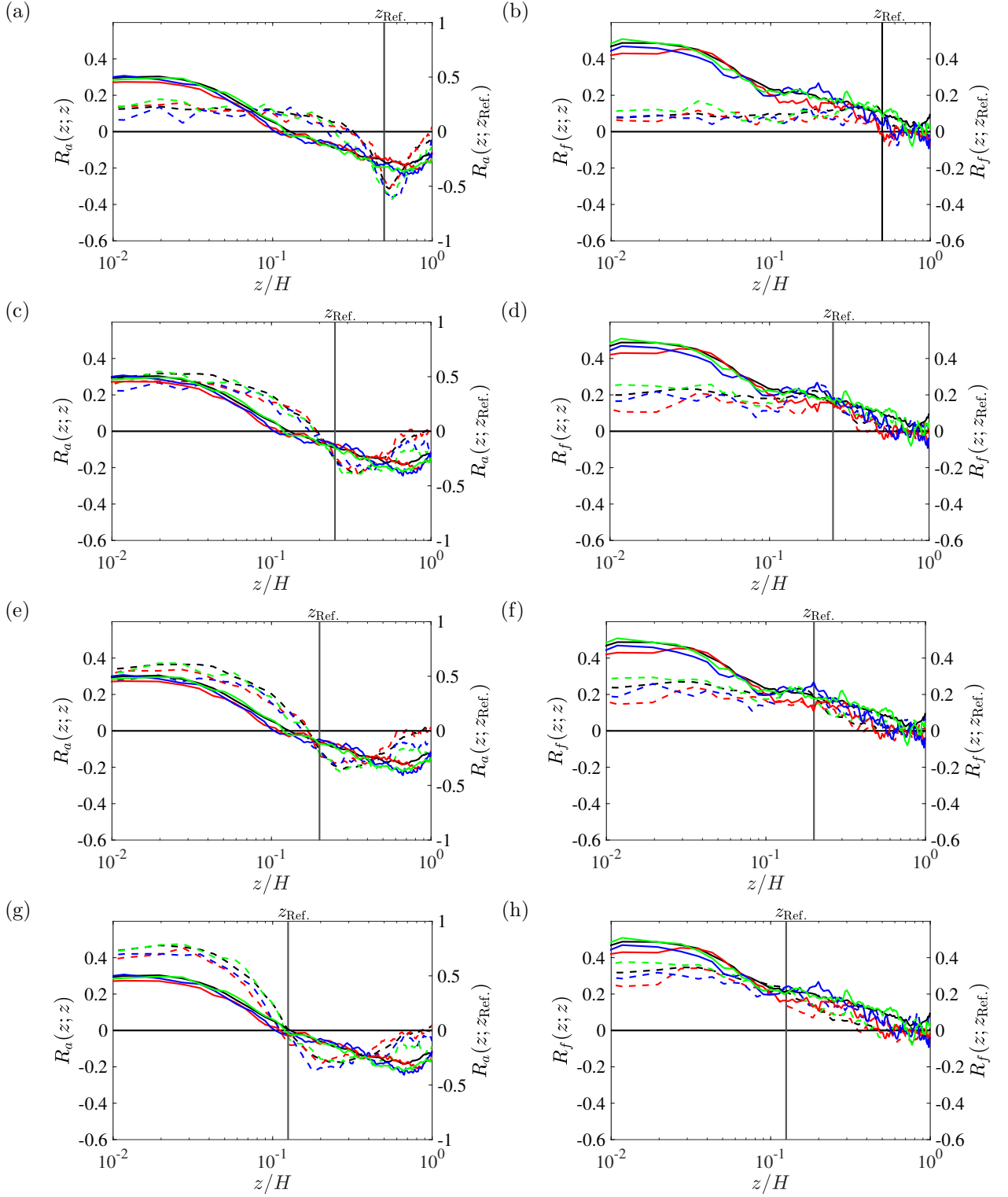


Figure 4.3: Amplitude and Frequency modulation correlation profiles. Panel correspond with: (a,c,e,g) R_a at $z_{\text{Ref.}} = 0.5, 0.25, 0.2, 0.125$, (b,d,f,h) R_f at $z_{\text{Ref.}} = 0.5, 0.25, 0.2, 0.125$; black: $L_x/H = 2\pi$, red: $L_x/H = 4\pi$, green: $L_x/H = 6\pi$ and blue: $L_x/H = 8\pi$; solid and dashed lines denote single- and two-point correlation respectively

CHAPTER 5

CONCLUSION

5.1 Conclusion

In this work I have used LES to study the effect of secondary flows driven and sustained due to spanwise topographic heterogeneity on amplitude and frequency modulation of small-scales near the wall. The topography under consideration is composed of two Gaussian mounds placed $2H$ apart, where H is the flow depth. All the results were compared against the benchmark case of homogeneous roughness. Even though the study was performed on a specific type of topographic arrangement, it can be replicated with any other type of surface complexity, given that the surface is capable of sustaining domain-scale secondary flows. Secondary flows and its effect on various turbulence statistics has received significant attention recently. Although, there have been different findings on the rotational sense of the vortices within the "low" and "high roughness" regions. This issue was addressed recently in the work of (Yang and Anderson, 2017; Vanderwel and Ganapathisubramani, 2015), it was shown that the spanwise spacing is an important parameter to determine the existence and scale of secondary flows. With these studies it was expected that the HMPs and LMPs should be flanked above the "high" and "low roughness" respectively.

In this study it was shown how the secondary flow enhances vertical mixing thereby diminishing the streamwise correlation within the HMP. The outer peak associated with the very large scale motions (VLSMs) vanishes within the HMP but is preserved within the LMP, which can be clearly observed with the pre-multiplied energy spectra. Although the peaks have been shifted to lower wavelengths within the LMP yet the overall turbulence statistics closely resemble with the homogeneous roughness case. This is an interesting finding since the LMPs and HMPs coexists due to same conditions, yet the LMPs appear less influential to the flow physics. Finally it was shown that even though a prominent secondary flow such

as in the present study alters the mean flow significantly yet it does not diminish inner-outer interaction. This study points out certain key observations that may have a significant contributions while developing a predictive model. One such observation is the importance of reference location while computing the two-point correlations for amplitude and frequency modulation. Therefore, the reference location should be carefully selected such that it passes through the region where an outer peak is observed. If such a condition is met, the single- and two-point correlation would very similar to each other for a wide range of domain height. The correlation profile for amplitude and frequency modulation were also compared for three different resolutions and were found to almost identical. The difference were negligible and may have arisen due to insufficient averaging time for high resolution cases.

To further explore the observation regarding the vanishing of outer peak within the HMPs for spanwise heterogeneous case I incorporated a study for domain length test. Upon observing the correlation profiles it was seen that even without a clear outer peak, the inner-outer interaction is not diminished. Hence, there arises a need to investigate how the correlation profiles are affected if the streamwise extent condition for the existence of VLSMs is not met. For this reason four cases with different domain length were studied and single- and two-point correlation were computed. The results showed that all the correlation profiles are identical irrespective of the domain length. This concludes that even if the conditions for the existence of VLSMs are not met there is essentially no effect on the correlation profiles. The results obtained in the entire study revolves around the amplitude and frequency modulating effect of the large scale structures residing in the log region on the small scale structures near the wall. Although numerous studies have been performed to study this interaction, yet there are still some areas which need significant attention. The predictive model that have been developed for obtain the statistics of small-scales near the wall are only tested on either a smooth-wall or some specific type of topographic arrangements. But in order to generalize the implementation of a predictive model other parameters that affects the modulation should also be taken into consideration.

REFERENCES

- Adrian, R. (2007). Hairpin vortex organization in wall turbulence. *Phys. Fluids* 19, 041301.
- Adrian, R., C. Meinhart, and C. Tomkins (2000). Vortex organization in the outer region of the turbulent boundary layer. *J. Fluid Mech.* 422, 1–54.
- Ahn, J., J. Lee, J. Lee, J.-H. Kang, and H. Sung (2015). Direct numerical simulation of a $30r$ long turbulent pipe flow at $re_\tau = 3008$. *Phys. Fluids* 27, 065110.
- Albertson, J. and M. Parlange (1999). Surface length scales and shear stress: implications for land-atmosphere interaction over complex terrain. *Water Resour. Res.* 35, 2121–2132.
- Anderson, W. (2012). An immersed boundary method wall model for high-reynolds number channel flow over complex topography. *Int. J. Numer. Methods Fluids* 71, 1588–1608.
- Anderson, W. (2016). Amplitude modulation of streamwise velocity fluctuations in the roughness sublayer: evidence from large-eddy simulations. *Journal of Fluid Mechanics* 789, 567588.
- Anderson, W., J. Barros, K. Christensen, and A. Awasthi (2015). Numerical and experimental study of mechanisms responsible for turbulent secondary flows in boundary layer flows over spanwise heterogeneous roughness. *J. Fluid Mech.* 768, 316–347.
- Anderson, W. and M. Chamecki (2014). Numerical study of turbulent flow over complex aeolian dune fields: The white sands national monument. *Physical Review E* 89, 013005–1–14.
- Anderson, W., Q. Li, and E. Bou-Zeid (2015). Numerical simulation of flow over urban-like topographies and evaluation of turbulence temporal attributes. *J. Turbulence* 16.
- Anderson, W. and C. Meneveau (2010). A large-eddy simulation model for boundary-layer flow over surfaces with horizontally resolved but vertically unresolved roughness elements. *Boundary-Layer Meteorol.* 137, 397–415.
- Anderson, W., P. Passalacqua, F. Porté-Agel, and C. Meneveau (2012). Large-eddy simulation of atmospheric boundary layer flow over fluvial-like landscapes using a dynamic roughness model. *Boundary-Layer Meteorol.* 144, 263–286.
- Antonia, R. A. and P.-. Krogstad (2001). Turbulence structure in boundary layers over different types of surface roughness. *Fluid Dynamics Research* 28(2), 139.
- Awasthi, A. and W. Anderson (2018, Apr). Numerical study of turbulent channel flow perturbed by spanwise topographic heterogeneity: Amplitude and frequency modulation within low- and high-momentum pathways. *Phys. Rev. Fluids* 3, 044602.

- Bandyopadhyay, P. and A. Hussain (1984). The coupling between scales in shear flows. *Phys. Fluids* 27, 2221–2228.
- Barros, J. M. and K. T. Christensen (2014). Observations of turbulent secondary flows in a rough-wall boundary layer. *Journal of Fluid Mechanics* 748.
- Boashash, B. (1992, 05). Estimating and interpreting the instantaneous frequency of a signalpart 1: Fundamentals. 80, 520 – 538.
- Bou-Zeid, E., C. Meneveau, and M. Parlange (2005). A scale-dependent lagrangian dynamic model for large eddy simulation of complex turbulent flows. *Phys. Fluids* 17, 025105.
- Bradshaw, P. (2003, 11). Turbulent secondary flows. 19, 53–74.
- Brundrett, E. and W. D. Baines (1964). The production and diffusion of vorticity in duct flow. *Journal of Fluid Mechanics* 19(3), 375394.
- Brunet, Y., J. J. Finnigan, and M. R. Raupach (1994, Jul). A wind tunnel study of air flow in waving wheat: Single-point velocity statistics. *Boundary-Layer Meteorology* 70(1), 95–132.
- Calaf, M., C. Meneveau, and J. Meyers (2010). Large eddy simulation study of fully developed wind-turbine array boundary layers. *Phys. Fluids* 22, 015110.
- Calaf, M., M. Parlange, and C. Meneveau (2011). Large eddy simulation study of scalar transport in fully developed wind-turbine array boundary layers. *Phys. Fluids* 23, 126603–16.
- Castro, I. (2007). Rough-wall boundary layers: mean flow universality. *J. Fluid Mech.* 585, 469–485.
- Castro, I. P., H. Cheng, and R. Reynolds (2006, Jan). Turbulence over urban-type roughness: Deductions from wind-tunnel measurements. *Boundary-Layer Meteorology* 118(1), 109–131.
- Chester, S., C. Meneveau, and M. Parlange (2007). Modelling of turbulent flow over fractal trees with renormalized numerical simulation. *J. Comp. Phys.* 225, 427–448.
- Coceal, O., A. Dobre, T. G. Thomas, and S. Belcher (2007). Structure of turbulent flow over regular arrays of cubical roughness. *J. Fluid Mech.* 589, 375–409.
- Cohen, L. (1989, Jul). Time-frequency distributions-a review. *Proceedings of the IEEE* 77(7), 941–981.
- De Graff, D. B. and J. K. Eaton (2000). Reynolds-number scaling of the flat-plate turbulent boundary layer. *Journal of Fluid Mechanics* 422, 319346.

- Fang, J. and F. Porté-Agel (2015). Large-eddy simulation of very-large-scale motions in the neutrally stratified atmospheric boundary layer. *Boundary-Layer Met.* 155, 397–416.
- Finnigan, J. (2000). Turbulence in plant canopies. *Ann. Rev. Fluid Mech.* 32, 519–571.
- Flack, K. and M. Schultz (2010). Review of hydraulic roughness scales in the fully rough regime. *ASME J. of Fluids Eng.* 132, 041203–1–10.
- Ganapathisubramani, B., E. K. Longmire, and I. Marusic (2003). Characteristics of vortex packets in turbulent boundary layers. *Journal of Fluid Mechanics* 478, 3546.
- George, W. K. (2007). Is there a universal log law for turbulent wall-bounded flows? *Philosophical Transactions of the Royal Society of London A: Mathematical, Physical and Engineering Sciences* 365(1852), 789–806.
- Germano, M. (1992, 06). Turbulence - the filtering approach. 238.
- Gessner, F. B. (1973). The origin of secondary flow in turbulent flow along a corner. *Journal of Fluid Mechanics* 58(1), 125.
- Goldstein, D. B. and T.-C. Tuan (1998, May). Secondary flow induced by riblets. *Journal of Fluid Mechanics* 363, 115–151.
- Graham, J. and C. Meneveau (2012). Modeling turbulent flow over fractal trees using renormalized numerical simulation: Alternate formulations and numerical experiments. *Phys. Fluids* 24, 125105.
- Grass, A. (1971). Structural features of turbulent flow over smooth and rough boundaries. *J. Fluid Mech.* 50, 233.
- Guala, M., M. Metzger, and B. J. McKeon (2011, 01). Interactions within the turbulent boundary layer at high reynolds number. 666.
- H.C. (1953). Essentials of fluid dynamics. by l. prandtl. london (blackie and son), 1952. pp. x, 452; many figures. 35s. *Quarterly Journal of the Royal Meteorological Society* 79(342), 570–570.
- Hellström, L., B. Ganapathisubramania, and A. Smits (2015). The evolution of large-scale motions in turbulent pipe flow. *J. Fluid Mech.* 779, 701–715.
- Hinze, J. O. (1967). Secondary currents in wall turbulence. *The Physics of Fluids* 10(9), S122–S125.
- Hong, J., J. Katz, C. Meneveau, and M. Schultz (2012). Coherent structures and associated subgrid-scale energy transfer in a rough-wall channel flow. *J. Fluid Mech.* 712, 92–128.

- Hoyas, S. and J. Jimnez (2006). Scaling of the velocity fluctuations in turbulent channels up to $Re=2003$. *Physics of Fluids* 18(1), 011702.
- Hutchins, N. and I. Marusic (2007a). Evidence of very long meandering features in the logarithmic region of turbulent boundary layers. *J. Fluid Mech.* 579, 1–28.
- Hutchins, N. and I. Marusic (2007b). Large-scale influences in near-wall turbulence. *Phil. Trans. R. Soc. A* 365, 647–664.
- Hutchins, N., T. Nickels, I. Marusic, and M. Chong (2009). Hot-wire spatial resolution issues in wall-bounded turbulence. *J. Fluid Mech.* 635, 103–136.
- J. Baars, W., M. K. Talluru, N. Hutchins, and I. Marusic (2015, 10). Wavelet analysis of wall turbulence to study large-scale modulation of small scales. 56.
- Jacob, C. and W. Anderson (2017, January). Conditionally Averaged Large-Scale Motions in the Neutral Atmospheric Boundary Layer: Insights for Aeolian Processes. *Boundary-Layer Meteorology* 162, 21–41.
- Jelly, T. O., S. Y. Jung, and T. A. Zaki (2014). Turbulence and skin friction modification in channel flow with streamwise-aligned superhydrophobic surface texture. *Physics of Fluids* 26(9), 095102.
- Jimenez, J. (2004). Turbulent flow over rough wall. *Annu. Rev. Fluid Mech.* 36, 173.
- Jimnez, J. and A. Pinelli (1999). The autonomous cycle of near-wall turbulence. *Journal of Fluid Mechanics* 389, 335359.
- Klewicki, J. C. and R. E. Falco (1990). On accurately measuring statistics associated with small-scale structure in turbulent boundary layers using hot-wire probes. *Journal of Fluid Mechanics* 219, 119142.
- Kline, S. J., W. C. Reynolds, F. A. Schraub, and P. W. Runstadler (1967). The structure of turbulent boundary layers. *Journal of Fluid Mechanics* 30(4), 741773.
- Krogstad, P.-A. and R. Antonia (1994). Structure of turbulent boundary layers on smooth and rough walls. *J. Fluid Mech.* 277, 1–21.
- Krogstad, P.-Å. and R. Antonia (1999, Oct). Surface roughness effects in turbulent boundary layers. *Experiments in Fluids* 27(5), 450–460.
- Leonardi, S., P. Orlandi, R. J. Smalley, L. Djenidi, and R. A. Antonia (2003). Direct numerical simulations of turbulent channel flow with transverse square bars on one wall. *Journal of Fluid Mechanics* 491, 229238.

- Marusic, I. and G. J. Kunkel (2003). Streamwise turbulence intensity formulation for flat-plate boundary layers. *Physics of Fluids* 15(8), 2461–2464.
- Mathis, R., N. Hutchins, and I. Marusic (2009a). Large-scale amplitude modulation of the small-scale structures in turbulent boundary layers. *J. Fluid Mech.* 628, 311–337.
- Mathis, R., N. Hutchins, and I. Marusic (2011). A predictive innerouter model for streamwise turbulence statistics in wall-bounded flows. *J. Fluid Mech.* 681, 537–566.
- Mathis, R., J. Monty, N. Hutchins, and I. Marusic (2009b). Comparison of large-scale amplitude modulation in turbulent boundary layers, pipes, and channel flows. *Phys. Fluids* 21, 111703.
- Meinhart, C. and R. Adrian (1995). On the existence of uniform momentum zones in a turbulent boundary layer. *Phys. Fluids* 7, 694–696.
- Mejia-Alvarez, R. and K. Christensen (2010). Low-order representations of irregular surface roughness and their impact on a turbulent boundary layer. *Phys. Fluids* 22, 015107.
- Mejia-Alvarez, R. and K. T. Christensen (2013). Wall-parallel stereo particle-image velocimetry measurements in the roughness sublayer of turbulent flow overlying highly irregular roughness. *Physics of Fluids* 25(11), 115109.
- Metzger, M. M. and J. C. Klewicki (2001). A comparative study of near-wall turbulence in high and low reynolds number boundary layers. *Physics of Fluids* 13(3), 692–701.
- Metzger, M. M., J. C. Klewicki, K. L. Bradshaw, and R. Sadr (2001). Scaling the near-wall axial turbulent stress in the zero pressure gradient boundary layer. *Physics of Fluids* 13(6), 1819–1821.
- Nezu, I. and H. Nakagawa (1993). *Turbulence in open-channel flows*. A.A. Balkema, Brookfield, VT.
- Nikuradse, J. (1933). Laws of flow in rough pipes. Technical Report 1292, NACA Tech. Mem.
- Pathikonda, G. and K. T. Christensen (2017, Apr). Inner[~]outer interactions in a turbulent boundary layer overlying complex roughness. *Phys. Rev. Fluids* 2, 044603.
- Perkins, H. J. (1970). The formation of streamwise vorticity in turbulent flow. *Journal of Fluid Mechanics* 44(4), 721740.
- Porte-Agel, F., C. Meneveau, and M. B. Parlange (2000). A scale-dependent dynamic model for large-eddy simulation: application to a neutral atmospheric boundary layer. *Journal of Fluid Mechanics* 415, 261284.

- Rao, K., R. Narasimha, and M. B. Narayanan (1971). The bursting phenomena in a turbulent boundary layer. *J. Fluid Mech.* 48, 339–352.
- Raupach, M., R. Antonia, and S. Rajagopalan (1991). Rough-wall turbulent boundary layers. *Appl. Mech. Rev.* 44, 1–25.
- Raupach, M., J. Finnigan, and Y. Brunet (1996). Coherent eddies and turbulence in vegetation canopies: the mixing layer analogy. *Boundary-Layer Meteorol.* 78, 351–382.
- Schultz, M. P. and K. A. Flack (2009). Turbulent boundary layers on a systematically varied rough wall. *Physics of Fluids* 21(1), 015104.
- Smagorinsky, J. (1963). General circulation experiments with the primitive equations. *Mon. Wea. Rev.* 91, 99–164.
- Stevens, R., M. Wilczek, and C. Meneveau (2014). Large-eddy simulation study of the logarithmic law for second- and higher-order moments in turbulent wall-bounded flow. *J. Fluid Mech.* 757, 888–907.
- Townsend, A. (1976). *The structure of turbulent shear flow*. Cambridge University Press, Cambridge, UK.
- Vanderwel, C. and B. Ganapathisubramani (2015). Effects of spanwise spacing on large-scale secondary flows in rough-wall turbulent boundary layers. *Journal of Fluid Mechanics* 774.
- Vermaas, D. A., W. S. J. Uijttewaai, and A. J. F. Hoitink (2011). Lateral transfer of streamwise momentum caused by a roughness transition across a shallow channel. *Water Resources Research* 47(2), n/a–n/a. W02530.
- Volino, R., M. Schultz, and K. Flack (2007). Turbulence structure in rough- and smooth-wall boundary layers. *J. Fluid Mech.* 592, 263–293.
- Wang, Z.-Q. and N.-S. Cheng (2005). Secondary flows over artificial bed strips. *Advances in Water Resources* 28(5), 441 – 450.
- Wilczek, M., R. Stevens, and C. Meneveau (2015). Spatio-temporal spectra in the logarithmic layer of wall turbulence: large-eddy simulations and simple models. *J. Fluid Mech.* 769, R1.
- Willingham, D., W. Anderson, K. T. Christensen, and J. Barros (2013). Turbulent boundary layer flow over transverse aerodynamic roughness transitions: induced mixing and flow characterization. *Phys. Fluids* 26, 025111–1–16.
- Wu, Y. and K. T. Christensen (2006). Population trends of spanwise vortices in wall turbulence. *Journal of Fluid Mechanics* 568, 5576.

- Wu, Y. and K. T. Christensen (2007). Outer-layer similarity in the presence of a practical rough-wall topology. *Phys. Fluids* 19, 085108.
- Wu, Y. and K. T. Christensen (2010). Spatial structure of a turbulent boundary layer with irregular surface roughness. *J. Fluid Mech.* 655, 380–418.
- Yang, J. and W. Anderson (2017, 08). Numerical study of turbulent channel flow over surfaces with variable spanwise heterogeneities: Topographically-driven secondary flows affect outer-layer similarity of turbulent length scales.

BIOGRAPHICAL SKETCH

Ankit Awasthi was born in Kanpur, U.P., India. He completed his schoolwork from Methodist High School, Kanpur, in 2009. Ankit entered Indian Institute of Information Technology, Jabalpur, in 2010 to pursue his bachelor's degree in Mechanical Engineering. Upon completing his bachelors in May 2014, Ankit entered The University of Texas at Dallas in the Mechanical Engineering graduate program. After completing his Master's degree in December 2016, Ankit continued his research at The University of Texas at Dallas to receive his doctorate degree in May 2018.

CURRICULUM VITAE

Ankit Awasthi

April, 2018

Contact Information:

Department of Mechanical Engineering Email: axa145430@utdallas.edu
The University of Texas at Dallas
Richardson, TX 75080-3021, U.S.A.

Educational History:

B.Tech., Mechanical Engineering, Indian Institute of Information Technology, Jabalpur, 2014
M.S., Mechanical Engineering, The University of Texas at Dallas, 2016
Ph.D., Mechanical Engineering, The University of Texas at Dallas, 2018

Ph.D. Dissertation

Mechanical Engineering Department, The University of Texas at Dallas
Advisors: Dr. William Anderson

Employment History:

Research Assistant, The University of Texas at Dallas, August 2015 – present

Publications:

Numerical study of turbulent channel flow perturbed by spanwise topographic heterogeneity: amplitude and frequency modulation within low- and high- momentum pathways, 2018, *Phys. Rev. Fluid* 3, Vol. 044602

Numerical and experimental study of mechanisms responsible for turbulent secondary flows in boundary layer flows over spanwise heterogeneous roughness, 2015, *J. Fluid Mech.*, Vol. 768

Professional Memberships:

American Physical Society, 2015–present